ARTICLE

https://doi.org/10.1038/s41586-018-0090-6

Diametric neural ensemble dynamics in parkinsonian and dyskinetic states

Jones G. Parker[1,2,9], Jesse D. Marshall[1,3,5,9], Biafra Ahanonu[1,3], Yu-Wei Wu[4], Tony Hyun Kim[1], Benjamin F. Grewe[1,6], Yanping Zhang[1,3], Jin Zhong Li[1,7], Jun B. Ding[4], Michael D. Ehlers[2,8]* & Mark J. Schnitzer[1,3]*

Loss of dopamine in Parkinson's disease is hypothesized to impede movement by inducing hypo- and hyperactivity in striatal spiny projection neurons (SPNs) of the direct (dSPNs) and indirect (iSPNs) pathways in the basal ganglia, respectively. The opposite imbalance might underlie hyperkinetic abnormalities, such as dyskinesia caused by treatment of Parkinson's disease with the dopamine precursor L-DOPA. Here we monitored thousands of SPNs in behaving mice, before and after dopamine depletion and during L-DOPA-induced dyskinesia. Normally, intermingled clusters of dSPNs and iSPNs coactivated before movement. Dopamine depletion unbalanced SPN activity rates and disrupted the movement-encoding iSPN clusters. Matching their clinical efficacy, L-DOPA or agonism of the D_2 dopamine receptor reversed these abnormalities more effectively than agonism of the D_1 dopamine receptor. The opposite pathophysiology arose in L-DOPA-induced dyskinesia, during which iSPNs showed hypoactivity and dSPNs showed unclustered hyperactivity. Therefore, both the spatiotemporal profiles and rates of SPN activity appear crucial to striatal function, and next-generation treatments for basal ganglia disorders should target both facets of striatal activity.

According to the classical rate model of Parkinson's disease, dSPNs and iSPNs normally have balanced activity rates, and the loss of dopamine induces an activity imbalance that suppresses movement by enhancing basal ganglia inhibition of the thalamo-cortical motor system[1–4]. The premise of the rate model, that the direct and indirect pathways are functionally opposed, concisely explained multiple aspects of basal ganglia function and dysfunction and led to descriptions of dystonia and Huntington's disease[1,2], Tourette's syndrome[5], dyskinesia[6], addiction[7], chronic pain[8], depression[9] and schizophrenia[10] based on imbalanced SPN activity rates. However, without cellular-level recordings that enable the comparison of dSPN and iSPN activity levels, no definitive evidence of a striatal activity imbalance has been shown in any of these conditions.

Optogenetic studies support the idea that dSPNs and iSPNs have opposing roles in movement initiation[11]. However, fluorescence recordings have recently shown that both cell types normally activate at movement onset with similar time courses[12–14]. These results challenge the rate model and reinvigorate models in which the direct and indirect pathways coordinate action selection by concurrently activating and suppressing competing motor programs, respectively[15]. The two pathways could still be opposed in some manner, but the oversimplicity of the rate model may underlie its inability to explain several notable features of Parkinson's disease[16], including the loss of movement-specific activity in nuclei downstream of the striatum[17]. Therefore, imbalanced SPN dynamics might only partially account for the motor symptoms of Parkinson's disease.

L-DOPA is the mainstay therapy for treating these symptoms, but whether it alters SPN activity and why it is superior to dopamine-receptor agonism remain unknown[18]. Notably, the efficacy of L-DOPA gradually decreases, as patients increasingly exhibit involuntary movements termed L-DOPA-induced dyskinesia (LID)[18]. Effective alternatives are needed to delay L-DOPA treatment and supplement or replace it upon loss of efficacy. LID is not fully understood, but might involve an activity imbalance opposite to that found in Parkinson's disease, with dSPN hyperactivity[19]. However, as with Parkinson's disease direct proof for these ideas has been lacking. To examine these issues, we compared dSPN and iSPN dynamics in freely behaving mice, under normal and parkinsonian conditions, before and after common treatments for Parkinson's disease and during LID.

Striatal encoding of movement

To selectively monitor dSPNs or iSPNs in the dorsomedial striatum, we respectively injected *Drd1a*^{cre} (*Drd1a* is also known as *Drd1*) or *Adora2a*^{cre} driver mice with a virus mediating Cre-dependent expression of the green-fluorescent Ca^{2+}-indicator GCaMP6m[20,21] (Methods). Control studies in live striatal tissue slices confirmed that somatic Ca^{2+} dynamics report spiking equivalently in dSPNs and iSPNs (Extended Data Fig. 1a–i).

To track SPN activity over weeks without affecting locomotor behaviour, we used a head-mounted microscope[22,23] and time-lapse microendoscopy[24] to image SPN dynamics as mice explored an open arena (Fig. 1 and Extended Data Fig. 1j, k). We computationally extracted activity traces of individual SPNs from the Ca^{2+} movies (262 ± 11 dSPNs (mean ± s.e.m.), 277 ± 8 iSPNs per mouse per session; 369 total 1-h-long sessions in 17 *Drd1a*^{cre} mice, 21 *Adora2a*^{cre} mice). Ca^{2+} transient events occurred at similar rates for dSPNs and iSPNs and had waveforms consistent with those in striatal slices (Extended Data Fig. 1l–n).

During movement, Ca^{2+} event rates rose markedly in both SPN types with similar dependencies on locomotor speed (Fig. 2a, b and Supplementary Videos 1, 2). Averaged over all Ca^{2+} events, locomotor speed rose after Ca^{2+} excitation with indistinguishable latencies in dSPNs and iSPNs (192 ± 9 ms (mean ± s.e.m.) and 196 ± 11 ms, respectively; $P = 0.8$; rank-sum test). Averaged over all movement bouts, mean SPN activity rose approximately 1 s before motion onset (Fig. 2c), with mean times to reach the half-maximum amplitude that were indistinguishable given the approximately 40-ms resolution of our statistical analysis (*Drd1a*^{cre} mice, -0.53 ± 0.04 s (mean ± s.e.m.)

[1]CNC Program, Stanford University, Stanford, CA, USA. [2]Neuroscience Research Unit, Pfizer Inc., Cambridge, MA, USA. [3]Howard Hughes Medical Institute, Stanford University, Stanford, CA, USA. [4]Department of Neurosurgery, Stanford University School of Medicine, Stanford, CA, USA. [5]Present address: Department of Organismic and Evolutionary Biology, Harvard University, Cambridge, MA, USA. [6]Present address: Institute of Neuroinformatics, University of Zürich and ETH Zürich, Zürich, Switzerland. [7]Present address: Cegeim Bio-Engineering (Changchun) Co. Ltd., Jilin, China. [8]Present address: Biogen, Cambridge, MA, USA. [9]These authors contributed equally: Jones G. Parker, Jesse D. Marshall. *e-mail: mschnitz@stanford.edu; michael.ehlers@biogen.com

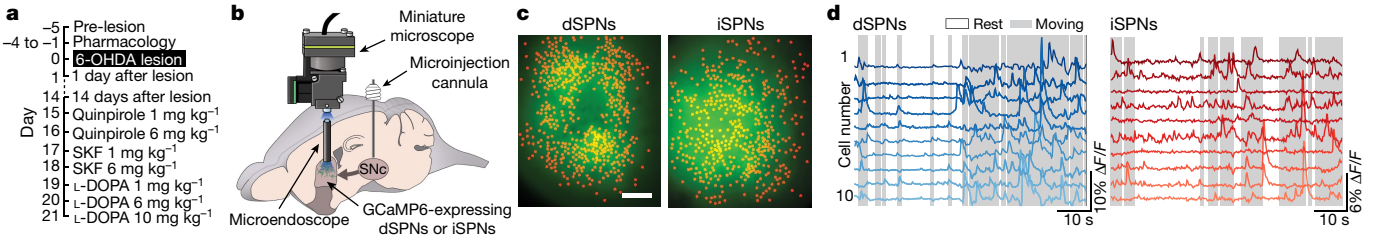

Fig. 1 | Ca^{2+} imaging of SPNs in freely behaving mice. a, Timeline of Ca^{2+} imaging sessions, 6-OHDA infusion and drug treatments. SKF, SKF81297. **b**, An Inscopix miniature microscope and microendoscope imaged SPN activity patterns. Infusion of 6-OHDA into substantia nigra (SNc) on day 0 ablated dopamine cells. **c**, Somata (red) of 573 dSPNs and 356 iSPNs in example *Drd1a*^{cre} (left) and *Adora2a*^{cre} (right) mice, atop mean fluorescence images of the dorsomedial striatum. Scale bar, 125 μm. **d**, Example Ca^{2+} activity traces in mice exploring an open arena. Grey shading, running periods; white shading, resting periods.

relative to motion onset, 17 mice, 5,372 cells, 2,899 movement bouts; *Adora2a*^{cre} mice, −0.48 ± 0.04 s, 21 mice, 5,880 cells, 3,559 movement bouts; $P = 0.7$; rank-sum test).

SPN activity was markedly clustered during movement, although the clusters of coactive cells were not absolutely stereotyped[14]. The spatial coordination of coactive SPNs rose and fell at motion onset and offset, respectively, with time courses that resembled those of the Ca^{2+} activity (Fig. 2c and Extended Data Fig. 2). Cell pairs within 100 μm or less were especially coactive, but beyond this distance pairwise activity correlations gradually decreased (Fig. 2d, e). By comparing the sets of cells that were activated during five different types of movement, we found that SPNs activated during bouts of the same movement type were, on average, more similar and closer together than those activated during different movement types[13] (Extended Data Fig. 3 and Methods).

To examine how dSPN and iSPN activity patterns were inter-related, we imaged their concurrent dynamics by two-photon microscopy in head-fixed mice in which both SPN-types expressed GCaMP6m and only dSPNs expressed the red-fluorescent marker tdTomato (Extended Data Fig. 4 and Supplementary Video 3). As the mice ran in place, dSPN and iSPN dynamics tracked locomotor behaviour indistinguishably. Nearby (20–100 μm) SPNs were equally coactive with other SPNs regardless of type, and the two cell populations encoded running speed equivalently.

Striatal activity after dopamine depletion

We next examined SPN dynamics in a classic model of Parkinson's disease[25]. Ipsilateral to the imaged striatum, we lesioned dopamine cells of the subtantia nigra pars compacta (SNc) using the neurotoxin 6-OHDA. Immunostaining for tyrosine hydroxylase, a marker of dopamine neurons, confirmed that the lesioned SNc lacked dopamine cell bodies 24 h after 6-OHDA infusion (Extended Data Fig. 5a, b). Following Ca^{2+} imaging, immunofluorescence intensities in the ipsilateral striatum more than 17 days after 6-OHDA infusion were 6 ± 1% (mean ± s.e.m.) of those contralateral to the lesion ($P = 6 \times 10^{-8}$; $n = 25$ mice; signed-rank test; Fig. 3a), verifying loss of dopamine neuron axons.

One day after the mice received 6-OHDA, locomotion was reduced relative to mice that had received saline infusions (Fig. 3b, c and Extended Data Fig. 5c). During Ca^{2+} imaging, background fluorescence was also reduced, but with almost no effect on the detection of Ca^{2+} events or SPNs (Extended Data Fig. 5d–h). Consistent with the rate model of Parkinson's disease, post-lesion (1 day) activity rates during rest and locomotion were decreased in dSPNs and increased in iSPNs compared to pre-lesion values (Fig. 3d–f and Extended Data Fig. 6). These effects resembled those of acute treatment with either D_1 dopamine receptor (D1R) or D_2 dopamine receptor (D2R) antagonists (Extended Data Fig. 7), which can cause parkinsonism in humans[26].

By 14 days after the lesion, a time point that may be more representative of the sustained dopamine depletion in patients with Parkinson's disease[27], locomotor activity had risen but remained below normal levels (Fig. 3c). iSPN activity remained elevated at baseline but barely rose at movement onset, no longer reflected locomotor speed and had lost nearly all of its spatial coordination (Fig. 3d–j). These abnormalities were also present during a rotarod assay of motor coordination (Extended Data Fig. 6c–e). The iSPN ensembles activated during different types of movement also became less distinctive after dopamine depletion, indicating reduced encoding specificity (Extended Data Fig. 8). By comparison, dSPN activity rates remained consistently depressed but still rose at motion onset and retained spatial coordination, a clear relationship to locomotion and selectivity for specific movement types (Fig. 3d–j). Thus, between acute and extended dopamine depletion, iSPN but not dSPN ensembles underwent pronounced changes in how their spatiotemporal dynamics encoded locomotion.

Treatment of aberrant neural dynamics

We next examined whether dopamine replacement or receptor agonism could reverse these aberrant SPN dynamics. Across days 15–20 after

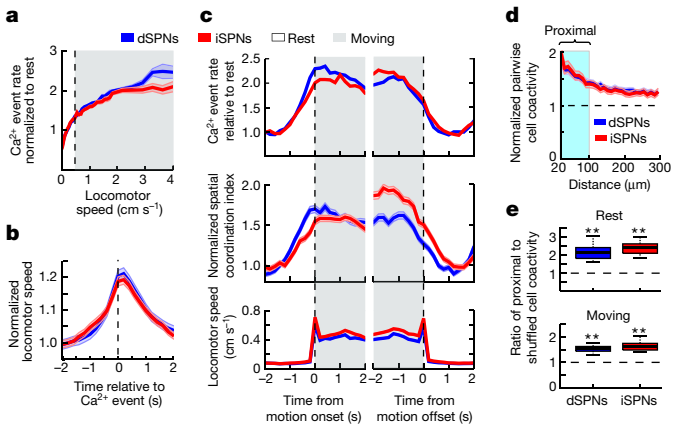

Fig. 2 | SPNs encode movement via spatially clustered bursts of activity. a, Mean SPN Ca^{2+} event rates versus running speed, relative to mean rates in resting mice (<0.5 cm s^{-1}). Grey shading denotes locomotion (>0.5 cm s^{-1}) in **a** and **c**. **b**, Mean speed relative to occurrences of Ca^{2+} events, normalized to mean speed 2 s before Ca^{2+} excitation. Traces are averages across all dSPNs (blue trace) and iSPNs (red trace). **c**, Mean speed (bottom), Ca^{2+} event rate (top) and spatial coordination of SPN activity (middle), relative to times of motion onset and offset. Top two traces are normalized to mean values in resting mice. Kinks in speed traces at motion onset/offset reflect the definition of a motion bout, for which the minimum speed to initiate a bout exceeds that to sustain one. **d**, Mean pairwise coactivity during locomotion versus the separation of cell pairs, normalized to values in temporally shuffled datasets (dashed line). Cyan, proximal (20–100 μm) cell pairs. **e**, Coactivity of proximal cell pairs exceeded that of the activity in shuffled datasets (**$P < 5 \times 10^{-4}$; signed-rank test comparing real and shuffled data; $n = 17$ *Drd1a*^{cre}, 21 *Adora2a*^{cre} mice). Exact P values can be found in the Supplementary Information for all figures. **a**–**e**, Data based on the same recordings (day −5; 17 *Drd1a*^{cre}, 21 *Adora2a*^{cre} mice). **a**–**d**, Colour shading indicates the s.e.m. **e**, In box-and-whisker plots, the horizontal lines denote median values, boxes cover the middle two quartiles and whiskers span 1.5× the interquartile range. Box-and-whisker plots in all other figures are formatted identically.

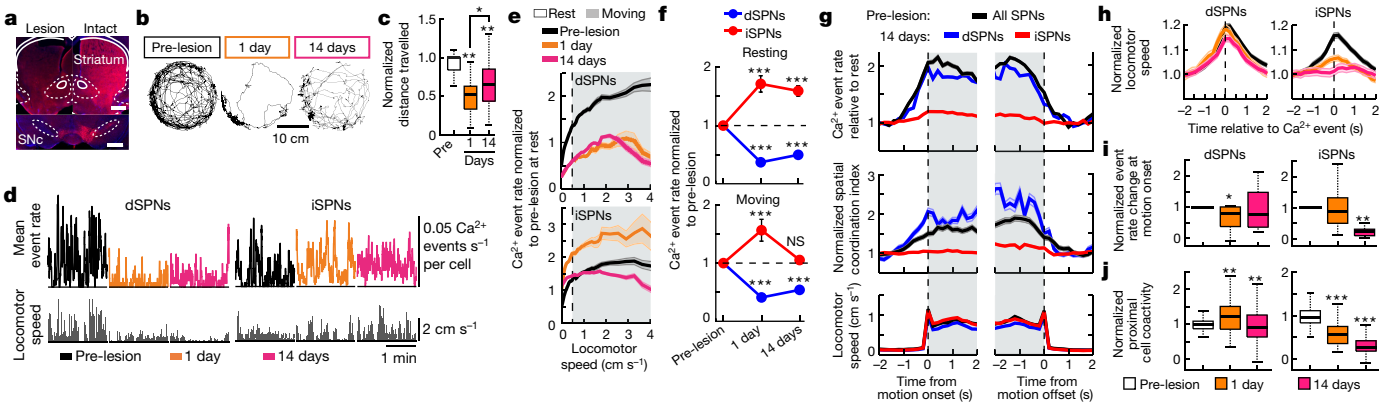

Fig. 3 | Dopamine loss differentially alters dSPN and iSPN activity patterns. a, Brain slices were immunostained for tyrosine hydroxylase (red) >14 days after unilateral 6-OHDA lesion and show unilateral loss of dopamine cell bodies and axons. White lines, brain area boundaries[38]. DAPI was used to stain the nuclei (blue). Scale bars, 1 mm. **b**, Example locomotor trajectories (15 min), before 6-OHDA lesion and 1 and 14 days after the lesion. **c**, Distance travelled, normalized for each mouse to its pre-lesion value. $^{**}P < 3 \times 10^{-3}$ compared to pre-lesion; $^{*}P = 0.013$ comparing 1 day to >14 days; signed-rank test, $n = 25$ mice. **d**, Traces of locomotor speed and mean Ca^{2+} event rate in example *Drd1a*^{cre} (left) and *Adora2a*^{cre} (right) mice, before (black), 1 day (orange) and 14 days (pink) after 6-OHDA lesion. **e**, Mean Ca^{2+} event rates versus speed, before and after 6-OHDA lesion, normalized to mean rates at rest (<0.5 cm s^{-1}) before the lesion. **f**, Ca^{2+} event rates (mean ± s.e.m.) before and after 6-OHDA lesion, normalized to pre-lesion values. $^{***}P < 5 \times 10^{-17}$; signed-rank test comparisons to pre-lesion; $n = 12$ *Drd1a*^{cre}, 13 *Adora2a*^{cre} mice. NS, not significant. **g**, Mean Ca^{2+} event rates (top), SPN spatial coordination (middle) and locomotor speed (bottom) relative to motion onset and offset, before and 14 days after 6-OHDA lesion. Given their similarity (Fig. 2c), pre-lesion traces for both SPN-types were combined. Traces are normalized to mean values from −2 s to −1 s relative to motion onset. Motion-related activity decreased in both SPN types after 6-OHDA lesion ($P = 10^{-61}$ (*Drd1a*^{cre}); $P = 10^{-111}$ (*Adora2a*^{cre})), but was more profoundly reduced in iSPNs. Rank-sum test; $n = 1{,}905$–$3{,}110$ motion bouts for both mouse lines at both time points. Spatial coordination of iSPN ($P = 10^{-9}$) but not dSPN activity ($P = 0.4$) decreased on day 14 to below pre-lesion values. $n = 1{,}326$–$2{,}957$ bouts with ≥2 active cells, for both mouse lines and time points; rank-sum test. **h**, Mean speeds relative to occurrences of Ca^{2+} events, normalized to values 2 s before Ca^{2+} excitation. At 14 days after 6-OHDA lesion, the mean speed rise within ±500 ms of a Ca^{2+} event was 0.8 ± 0.3% (mean ± s.e.m.) for iSPNs, 11 ± 1% for dSPNs. $n = 3{,}498$–$5{,}529$ cells per day, for both mouse lines. **i**, Rises in Ca^{2+} event rates at motion onset, based on data from **g**. For each group, we averaged over all movement bouts and compared the event rates during the intervals −2 to −1 s before and 0–1 s after motion onset. Values normalized to the pre-lesion values. $^{*}P = 0.03$; $^{**}P = 9 \times 10^{-7}$; rank-sum test compared to pre-lesion values; $n = 12$ *Drd1a*^{cre} and 13 *Adora2a*^{cre} mice. **j**, Coactivity values in proximal SPN pairs (20–100 μm apart) during locomotion, after subtraction of coactivity values in shuffled datasets. Values normalized to pre-lesion values. $^{**}P < 2 \times 10^{-4}$; $^{***}P < 4 \times 10^{-12}$; rank-sum test comparing pre-lesion to 1 day and >14 days; $n = 96$–416 coactivity values for both mouse lines and all three time points. **c**, **e**–**j**, Data are from the same 12 *Drd1a*^{cre} and 13 *Adora2a*^{cre} mice. **e**, **g**, **h**, Colour shading indicates the s.e.m. Pre-lesion data were acquired on day −5. Data for >14 days were from 1-h recordings on day 14 plus 30-min recordings on days 15, 17 and 20 performed after saline vehicle administration but before drug treatment.

6-OHDA infusion, we successively administered 1 or 6 mg kg^{-1} of a D2R agonist (quinpirole), a D1R agonist (SKF81297), or L-DOPA. As in past work using the 6-OHDA model of Parkinson's disease, these agents induced locomotor turning contralateral to the lesioned SNc[25], to equipotent levels within the tested dosage ranges (Fig. 4a and Extended Data Fig. 9a–e).

All three drugs also increased dSPN activity, unexpectedly so for quinpirole, given the lack of D2Rs on dSPNs[28,29] (Fig. 4b–d). Quinpirole and the 6 mg kg^{-1} L-DOPA dose, but not SKF81297, further ameliorated the activity imbalance by reducing the elevated iSPN activity in resting mice. The two agonists had divergent effects from those in normal mice, in which they both unexpectedly depressed SPN activity (Extended Data Fig. 7d–f and Supplementary Note). Given the unilateral lesion and systemic drug administration, drug effects in the contralateral striatum or even outside striatum could contribute to these observations, although the brain's greatest densities of dopaminergic inputs and dopamine receptors are in the striatum[30].

Beyond rebalancing SPN activity, L-DOPA mostly restored the coupling to locomotion and spatial clustering of iSPN activity (Fig. 4b, e–i). D2R agonism failed to restore the iSPN activity rise at motion onset, whereas D1R agonism rescued neither the elevated rates nor spatial clustering of iSPN activity (Fig. 4c, f–i). Thus, although L-DOPA and both agonists reversed the activity imbalance, only L-DOPA reversed the deficits in both motion-related iSPN activity and its spatial coordination. These differences in treating neural abnormalities arose even at doses equally affecting turning behaviour, the standard metric of therapeutic efficacy in this model of Parkinson's disease[25].

Late in the treatment of Parkinson's disease, patients commonly develop LID, which we modelled by giving parkinsonian mice a dyskinesiogenic (10 mg kg^{-1}) L-DOPA dose[31] that induced abnormal facial, limb and trunk movements (Extended Data Fig. 9f–j). During dyskinesia, dSPNs were hyperactive and iSPNs hypoactive. Furthermore, dSPNs lost their spatial coordination and movement-evoked responses, whereas iSPNs became more responsive to motion onset (Fig. 5). Thus, the signature dSPN and iSPN dynamics in parkinsonian and dyskinetic states were diametric opposites of each other (Supplementary Video 4). This anti-symmetry provides an attractive explanation for the opposite motor symptoms of Parkinson's disease and LID.

Implications for basal ganglia function

Our data show dSPNs and iSPNs normally have indistinguishable kinetics at motion onset and offset[12] (Fig. 2), challenging the idea that the two cell types respectively mark movement start and end[32]. Activation patterns in the two SPN types were comparably clustered, consistent with previous reports[13,14]. Supporting one recent study[13], the clusters of active SPNs that we identified were neither absolutely stereotyped nor spatially compact.

The ensemble activity that we observed in both SPN types precisely encoded locomotor speed (Extended Data Fig. 4l, m) and as in recent work[13] arose in clusters that preferentially encoded specific movement types (Extended Data Fig. 3, 10). Simultaneous Ca^{2+} imaging in both SPN types revealed interspersed patterns of dSPN and iSPN activity (Extended Data Fig. 4j, k). Together, these findings pose a challenge to 'suppression–selection' models[15], in which the main iSPN function is to broadly suppress competing actions other than the one selected. Such models predict that iSPN dynamics should be less selective, more diffuse and perhaps less velocity-sensitive than those of dSPNs. Instead,

it appears that iSPNs and dSPNs jointly engage in movement selection via synchronized activation in interspersed cell clusters of comparable size coupled indistinguishably to locomotion. The data here come from the dorsomedial striatum, and future work should explore whether the findings generalize to other striatal regions.

The spatial extent of dSPN and iSPN coactivation resembles that of corticostriatal neurons with focal axonal arborizations (around 100–300 μm wide) within the rodent striatal matrix[33]. Striatal areas receiving these projections are termed matrisomes and have somatotopically organized cortical inputs and projections to basal ganglia output nuclei[34]. Thus, the spatiotemporal organization of cortical input and the convergence of signals from the direct and indirect pathways are probably both vital for sculpting the motor output signals of the basal ganglia[15,32,35] (Extended Data Fig. 11).

Signatures of a parkinsonian state

The notion that an excess or deficiency of dopamine signalling unbalances striatal dynamics has long provided the conceptual basis for treating basal ganglia disorders[1,2,5–10], but direct evidence of imbalanced striatal activity has been lacking. We uncovered opposite imbalances in dorsomedial striatum after dopamine depletion and LID, and additional facets of SPN pathophysiology that probably contribute to the symptoms of Parkinson's disease, their reversal by dopamine restoration, and the hyperkinesia of LID.

We found four distinct signatures of a parkinsonian state: reduced spontaneous dSPN activity; increased spontaneous iSPN activity; reduced coupling of iSPN activity levels to motion onset and offset; and decreased spatial clustering of iSPN activity (Extended Data Fig. 11). Collectively, these signatures expose the incompleteness of the rate model. Notwithstanding, these findings support the model's predictions for how spontaneous rates of SPN activity change in Parkinson's disease. Abnormal rates of spontaneous SPN activity may indeed impede movement by increasing activity in the inhibitory output projections of the basal ganglia. The loss of spatially clustered iSPN activity and its coupling to movement lie beyond the rate model and probably also contribute to parkinsonian symptoms. These unexpected deficits might indicate disruptions to matrisome[33,34] function that preclude the spatiotemporal dynamics required in basal ganglia output nuclei for well-choreographed actions. The added deficits did not arise after acute dopamine depletion or D1R or D2R antagonism and are consistent with electrophysiological recordings in a genetic mouse model of progressive dopamine cell loss[36].

These progressive pathophysiologic changes probably reflect neural adaptations that occur during chronic dopamine depletion, many of which preferentially affect iSPNs, such as reduced dendritic spine density and increased input from inhibitory interneurons (Supplementary Note). Notably, the long-term adaptations in SPN dynamics were precisely those best treated by L-DOPA and D2R agonism. The mechanisms by which these treatments immediately counteracted the long-term facets of SPN pathophysiology are unclear but important to identify, because the capabilities of the different compounds for reversing the neural abnormalities matched their clinical utilities[18] (in order of efficacy: L-DOPA, D2R agonism, D1R agonism) and might underlie the varying utility of dopamine agonist monotherapy versus that of L-DOPA in different stages of Parkinson's disease[37].

Anti-symmetric deficits in LID

Notably, during LID the dorsomedial striatum exhibits diametric abnormalities to those in the parkinsonian state. Dyskinesia is characterized by decreased spontaneous iSPN activity, increased spontaneous dSPN activity and a loss of spatially clustered and movement-coupled dSPN activity. These features are the polar opposite of those of the parkinsonian state and may explain the opposite motor symptoms of the two conditions. They also fit with reported cellular adaptations in Parkinson's disease versus LID, including reductions of dendritic spines on iSPNs and dSPNs, respectively[19,27]. A caveat is that we examined a model of acute LID, which differs from models with more prolonged

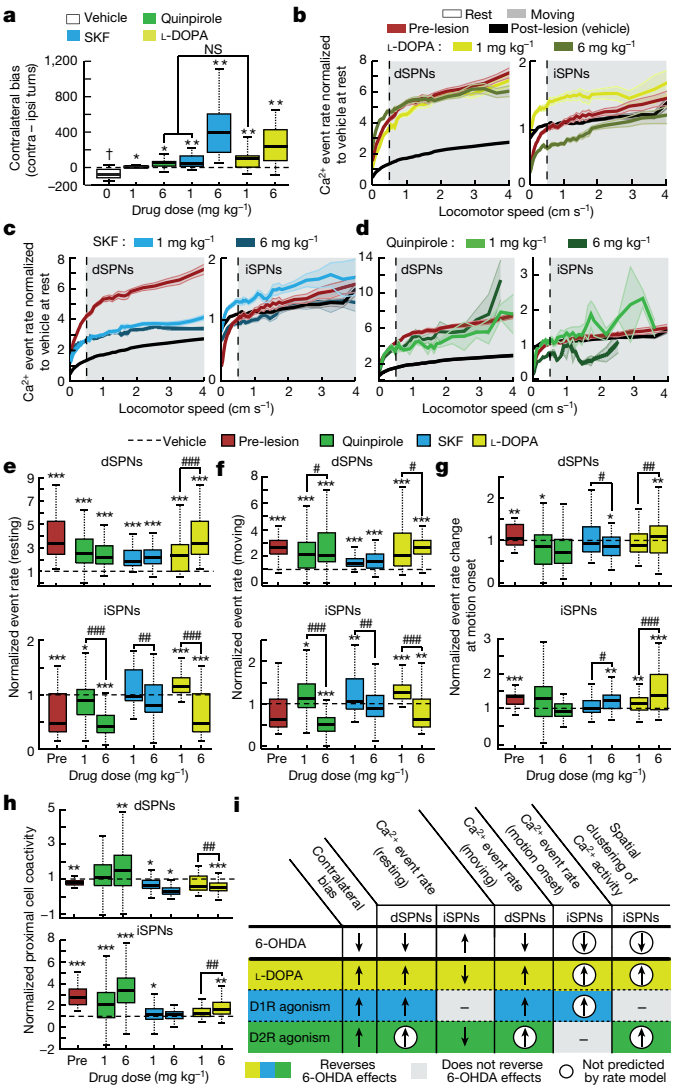

Fig. 4 | L-DOPA better reversed the deficits in SPN activity than dopamine receptor agonism. a, Contralateral turning bias during 40-min periods of locomotion, >14 days after 6-OHDA lesion, after administration of saline vehicle, or 1 mg kg^{-1} or 6 mg kg^{-1} D2R agonist (quinpirole), D1R agonist (SKF81297) or L-DOPA. $n = 13$ mice; one treatment per day, in the order stated. **b**–**d**, Mean SPN Ca^{2+} event rates versus locomotor speed, under different treatment conditions (days 15–21 after 6-OHDA lesion). Values were normalized to mean event rates in mice at rest (<0.5 cm s^{-1}) after saline injection. Colour shading indicates s.e.m. **b**–**h**, Data are from the same 7 *Drd1a*^{cre}, 6 *Adora2a*^{cre} mice. **e**, **f**, Ca^{2+} event rates when mice were resting (**e**) or moving (**f**). Values in **e**–**h** were normalized for each mouse to measured values after saline treatment and 6-OHDA lesion (dashed lines). $n = 14$ speed bins <0.5 cm s^{-1}, $n = 24$ speed bins >0.5 cm s^{-1}, $n = 7$ *Drd1a*^{cre}, 6 *Adora2a*^{cre} mice. **g**, Increases in Ca^{2+} event rates at motion onset. For each treatment, we averaged over all motion bouts and computed the mean rate 0–2 s after motion onset, normalized to rates from −2 to −1 s before motion onset (dashed lines). $n = 11$ time bins per mouse per treatment. **h**, Coactivity in proximal SPN pairs (20–100 μm apart) during movement, after subtracting coactivity values in shuffled datasets. $n = 8$ bins of cell–cell separation, $n = 7$ *Drd1a*^{cre}, 6 *Adora2a*^{cre} mice. **i**, Summary of effects. Arrows indicate mean changes of ≥10% at the 6 mg kg^{-1} dose of each drug. Encircled arrows indicate effects unpredicted by the rate model of Parkinson's disease. Statistical tests are signed-rank tests with Dunn–Sidak correction for multiple comparisons. †$P = 2.4 \times 10^{-3}$ for comparisons to pre-lesion; *$P < 6 \times 10^{-3}$, **$P < 6 \times 10^{-4}$, ***$P < 6 \times 10^{-7}$ for comparisons to vehicle treatment; #$P < 0.05$, ##$P < 5 \times 10^{-3}$, ###$P < 5 \times 10^{-7}$ for comparisons between drug doses. Pre-lesion data were acquired on day −5. Vehicle data were aggregated for 30-min recordings on days 15–21 after saline administration but before drug treatment.

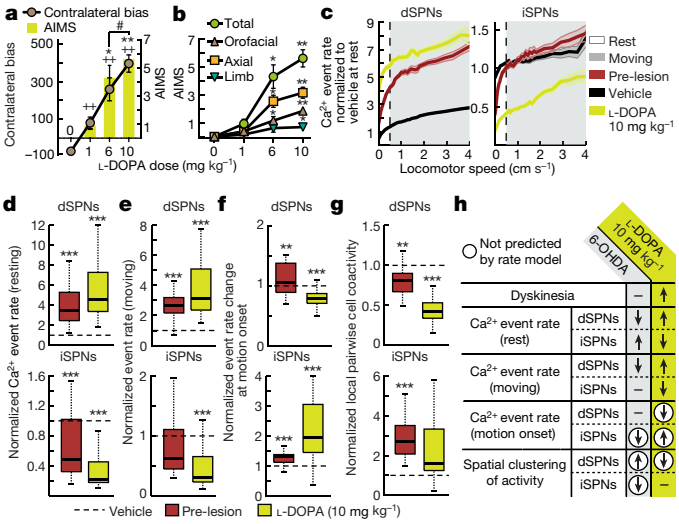

Fig. 5 | In LID, iSPNs are hypoactive and dSPNs have uncorrelated patterns of hyperactivity. a, Turning bias (mean ± s.e.m.) and abnormal involuntary movement score (AIMS) within 40 min after saline vehicle or L-DOPA injection, >14 days after 6-OHDA lesion. $\#\#P < 10^{-3}$ for comparisons of contralateral bias to vehicle treatment; signed-rank test; $*P = 10^{-2}$ and $**P = 10^{-4}$ comparing AIMS values to those after vehicle treatment; rank-sum test; $n = 13$ mice. 10 mg kg^{-1} L-DOPA induced higher AIMS values than 6 mg kg^{-1}. $\#P = 0.013$; signed-rank test. **b**, Peak AIMS (mean ± s.e.m.), separated by movement type, within 40 min after vehicle or L-DOPA treatment in mice >14 days after 6-OHDA lesion. $*P < 0.05$, $**P < 5 \times 10^{-3}$ for comparisons to vehicle treatment; rank-sum test; $n = 13$ mice. **c**, Mean SPN Ca^{2+} event rates versus locomotor speed before 6-OHDA lesion, and >14 days after the lesion following either vehicle or 10 mg kg^{-1} L-DOPA treatment. Values are normalized to mean rates when mice were resting (<0.5 cm s^{-1}) after vehicle treatment. Grey shading indicates >0.5 cm s^{-1} locomotion. Colour shading indicates the s.e.m. **c**–**g**, Data are from the same 7 *Drd1a*^{cre}, 6 *Adora2a*^{cre} mice. **d**, **e**, Ca^{2+} event rates when mice were resting (<0.5 cm s^{-1}; **d**) or moving (>0.5 cm s^{-1}; **e**). All values in **d**–**g** are normalized to those after vehicle treatment in lesioned mice (dashed lines). Statistical tests in **d**–**g** are signed-rank tests with Dunn–Sidak correction for multiple comparisons. $*P < 6 \times 10^{-3}$, $**P < 6 \times 10^{-4}$, $***P < 6 \times 10^{-7}$ for comparisons to vehicle treatment. $n = 14$ speed bins <0.5 cm s^{-1}, 24 speed bins >0.5 cm s^{-1} for all 13 mice. **f**, Rises in Ca^{2+} event rates at motion onset. For each treatment, we averaged over all motion bouts and computed the mean rate 0–2 s after motion onset, relative to the values from −2 to −1 s before onset. $n = 11$ time bins per mouse per treatment. **g**, Coactivity in proximal SPN pairs (20–100 μm apart) during movement, after subtracting coactivity values in shuffled datasets. $n = 8$ bins of cell–cell separation per mouse. **h**, Summary of effects. Arrows indicate mean changes ≥10%. Encircled arrows indicate effects unpredicted by the classical rate model. Pre-lesion data were acquired on day −5. Vehicle data aggregates 30-min recordings on days 15–21 were acquired after vehicle administration but before drug treatment.

courses of L-DOPA treatment known to induce a range of cellular adaptations[27].

As with uncorrelated iSPN hyperactivity in the parkinsonian state, uncorrelated dSPN hyperactivity in LID probably also disrupts movement selection, but in this case causing excessive, unplanned movements. However, it remains unclear whether and how dSPN activity patterns relate to specific dyskinetic movements. Just as pharmacological restoration of spatially coordinated iSPN activity was associated with clinical efficacy in treating the symptoms of Parkinson's disease, reversing or preventing the loss of spatially coordinated dSPN activity in LID might benefit patients with late-stage Parkinson's disease. Overall, the distinctive neural signatures of Parkinson's disease and LID established here may provide biomarkers facilitating development of substitutes for L-DOPA or treatment regimens extending its period of efficacy.

Beyond Parkinson's disease and dyskinesia, our results provide the impetus and means for testing whether other basal ganglia disorders unbalance striatal activity and disrupt its coding dynamics[5,7–10]. As with Parkinson's disease and LID, it is probable that ideas beyond the rate model framework will be required to explain the spectrum of basal ganglia abnormalities and patient symptoms. Current treatment approaches often aim to correct activity imbalances, but our results indicate that next-generation therapies should also target the concomitant biological adaptations that disrupt striatal neural ensemble coding.

Online content

Any Methods, including any statements of data availability and Nature Research reporting summaries, along with any additional references and Source Data files, are available in the online version of the paper at https://doi.org/10.1038/s41586-018-0090-6.

Received: 30 May 2016; Accepted: 27 March 2018;
Published online 2 May 2018.

1. Albin, R. L., Young, A. B. & Penney, J. B. The functional anatomy of basal ganglia disorders. *Trends Neurosci.* **12**, 366–375 (1989).
2. DeLong, M. R. Primate models of movement disorders of basal ganglia origin. *Trends Neurosci.* **13**, 281–285 (1990).
3. Shen, W., Flajolet, M., Greengard, P. & Surmeier, D. J. Dichotomous dopaminergic control of striatal synaptic plasticity. *Science* **321**, 848–851 (2008).
4. Mallet, N., Ballion, B., Le Moine, C. & Gonon, F. Cortical inputs and GABA interneurons imbalance projection neurons in the striatum of parkinsonian rats. *J. Neurosci.* **26**, 3875–3884 (2006).
5. Castellan Baldan, L. C. et al. Histidine decarboxylase deficiency causes Tourette syndrome: parallel findings in humans and mice. *Neuron* **81**, 77–90 (2014).
6. Jenner, P. Molecular mechanisms of l-DOPA-induced dyskinesia. *Nat. Rev. Neurosci.* **9**, 665–677 (2008).
7. Lobo, M. K. et al. Cell type-specific loss of BDNF signaling mimics optogenetic control of cocaine reward. *Science* **330**, 385–390 (2010).
8. Schwartz, N. et al. Decreased motivation during chronic pain requires long-term depression in the nucleus accumbens. *Science* **345**, 535–542 (2014).
9. Francis, T. C. et al. Nucleus accumbens medium spiny neuron subtypes mediate depression-related outcomes to social defeat stress. *Biol. Psychiatry* **77**, 212–222 (2015).
10. Moore, H., West, A. R. & Grace, A. A. The regulation of forebrain dopamine transmission: relevance to the pathophysiology and psychopathology of schizophrenia. *Biol. Psychiatry* **46**, 40–55 (1999).
11. Kravitz, A. V. et al. Regulation of parkinsonian motor behaviours by optogenetic control of basal ganglia circuitry. *Nature* **466**, 622–626 (2010).
12. Cui, G. et al. Concurrent activation of striatal direct and indirect pathways during action initiation. *Nature* **494**, 238–242 (2013).
13. Klaus, A. et al. The spatiotemporal organization of the striatum encodes action space. *Neuron* **95**, 1171–1180 (2017).
14. Barbera, G. et al. Spatially compact neural clusters in the dorsal striatum encode locomotion relevant information. *Neuron* **92**, 202–213 (2016).
15. Mink, J. W. The basal ganglia: focused selection and inhibition of competing motor programs. *Prog. Neurobiol.* **50**, 381–425 (1996).
16. Galvan, A. & Wichmann, T. Pathophysiology of Parkinsonism. *Clin. Neurophysiol.* **119**, 1459–1474 (2008).
17. Bronfeld, M. & Bar-Gad, I. Loss of specificity in basal ganglia related movement disorders. *Front. Syst. Neurosci.* **5**, 38 (2011).
18. Jankovic, J. & Aguilar, L. G. Current approaches to the treatment of Parkinson's disease. *Neuropsychiatr. Dis. Treat.* **4**, 743–757 (2008).
19. Cenci, M. A. & Konradi, C. Maladaptive striatal plasticity in l-DOPA-induced dyskinesia. *Prog. Brain Res.* **183**, 209–233 (2010).
20. Chen, T. W. et al. Ultrasensitive fluorescent proteins for imaging neuronal activity. *Nature* **499**, 295–300 (2013).
21. Gong, S. et al. Targeting Cre recombinase to specific neuron populations with bacterial artificial chromosome constructs. *J. Neurosci.* **27**, 9817–9823 (2007).
22. Ghosh, K. K. et al. Miniaturized integration of a fluorescence microscope. *Nat. Methods* **8**, 871–878 (2011).
23. Ziv, Y. et al. Long-term dynamics of CA1 hippocampal place codes. *Nat. Neurosci.* **16**, 264–266 (2013).
24. Barretto, R. P. et al. Time-lapse imaging of disease progression in deep brain areas using fluorescence microendoscopy. *Nat. Med.* **17**, 223–228 (2011).
25. Schwarting, R. K. & Huston, J. P. The unilateral 6-hydroxydopamine lesion model in behavioral brain research. Analysis of functional deficits, recovery and treatments. *Prog. Neurobiol.* **50**, 275–331 (1996).
26. Montastruc, J. L., Llau, M. E., Rascol, O. & Senard, J. M. Drug-induced Parkinsonism: a review. *Fundam. Clin. Pharmacol.* **8**, 293–306 (1994).
27. Fieblinger, T. et al. Cell type-specific plasticity of striatal projection neurons in Parkinsonism and l-DOPA-induced dyskinesia. *Nat. Commun.* **5**, 5316 (2014).
28. Gerfen, C. R. et al. D_1 and D_2 dopamine receptor-regulated gene expression of striatonigral and striatopallidal neurons. *Science* **250**, 1429–1432 (1990).
29. Gong, S. et al. A gene expression atlas of the central nervous system based on bacterial artificial chromosomes. *Nature* **425**, 917–925 (2003).

30. Bentivoglio, M. & Morelli, M. in *Handbook of Chemical Neuroanatomy* Vol. 21 (eds Dunnett, S. B. et al.) 1–107 (Elsevier, Amsterdam, 2005).
31. Cenci, M. A. & Lundblad, M. Ratings of l-DOPA-induced dyskinesia in the unilateral 6-OHDA lesion model of Parkinson's disease in rats and mice. *Curr. Protoc. Neurosci.* **41**, 9.25.1–9.25.23 (2007).
32. Hikosaka, O., Takikawa, Y. & Kawagoe, R. Role of the basal ganglia in the control of purposive saccadic eye movements. *Physiol. Rev.* **80**, 953–978 (2000).
33. Kincaid, A. E. & Wilson, C. J. Corticostriatal innervation of the patch and matrix in the rat neostriatum. *J. Comp. Neurol.* **374**, 578–592 (1996).
34. Graybiel, A. M., Aosaki, T., Flaherty, A. W. & Kimura, M. The basal ganglia and adaptive motor control. *Science* **265**, 1826–1831 (1994).
35. Alexander, G. E. & Crutcher, M. D. Functional architecture of basal ganglia circuits: neural substrates of parallel processing. *Trends Neurosci.* **13**, 266–271 (1990).
36. Panigrahi, B. et al. Dopamine is required for the neural representation and control of movement vigor. *Cell* **162**, 1418–1430 (2015).
37. Perez-Lloret, S. & Rascol, O. Dopamine receptor agonists for the treatment of early or advanced Parkinson's disease. *CNS Drugs* **24**, 941–968 (2010).
38. Paxinos, G. & Franklin, K. B. *The Mouse Brain in Stereotaxic Coordinates* (Academic, San Diego, 2001).

Acknowledgements We appreciate support from HHMI, the Stanford CNC Program, Stanford Photonics Research Center, Pfizer and a GG Technologies gift fund; fellowships from Stanford (J.D.M., T.H.K.), the Helen Hay Whitney Foundation (J.D.M.), the US National Institutes of Health (J.G.P., J.B.D.), HHMI (B.A.), the US National Science Foundation (B.A.), the Bill & Melinda Gates Foundation (B.A.), and the Swiss National Science Foundation (B.F.G.). We thank L. Burns, L. Kitch, E. Hamel, J. Lecoq, M. Larkin, T. Fieblinger, S. Ganguli, A. Girasole, A. Graybiel, A. Kreitzer, R. Malenka and A. Nelson for technical assistance and discussion, Inscopix Inc. for technical support and upgrades, and B. Rossi for scientific illustration.

Reviewer information *Nature* thanks D. Surmeier, G. Stuber and the other anonymous reviewer(s) for their contribution to the peer review of this work.

Author contributions J.G.P., J.D.M., M.D.E. and M.J.S. designed experiments and analyses. J.G.P., J.D.M., B.F.G. and T.H.K. established in vivo imaging protocols and performed experiments. J.D.M., J.G.P. and B.A. analysed data. J.Z.L. and Y.Z. constructed the viral vectors. Y.-W.W. and J.B.D. performed and analysed in vitro electrophysiological recordings. J.G.P., J.D.M. and M.J.S. wrote the paper. M.D.E. and all other authors edited the paper. M.D.E. and M.J.S. supervised the research.

Competing interests M.J.S. is a scientific cofounder of Inscopix, Inc., which produces the miniature fluorescence microscope used in this study. M.D.E. and J.G.P. were Pfizer employees during the initial part of the project.

Additional information
Extended data is available for this paper at https://doi.org/10.1038/s41586-018-0090-6.
Supplementary information is available for this paper at https://doi.org/10.1038/s41586-018-0090-6.
Reprints and permissions information is available at http://www.nature.com/reprints.
Correspondence and requests for materials should be addressed to M.D.E. and M.J.S.
Publisher's note: Springer Nature remains neutral with regard to jurisdictional claims in published maps and institutional affiliations.

METHODS

Mice. We obtained the GENSAT BAC-transgenic Cre-driver mouse lines, *Drd1a*^{cre} (FK150) and *Adora2a*^{cre} (KG139), from the Mutant Mouse Research & Resource Centers (https://www.mmrrc.org). We crossed these mice with wild-type C57BL/6 mice. We inbred the resulting heterozygous offspring to generate homozygous BAC-transgenic animals, which we maintained through further homozygous crosses. To generate mice for our two-photon imaging experiments, we crossed homozygous *Drd1a*^{cre} with homozygous reporter mice (*Ai14* (also known as *Gt(ROSA)26Sor*$^{tm14(CAG-tdTomato)Hze}$ mice); Allen Brain Institute) expressing the red fluorophore tdTomato in a Cre-dependent manner. We used both male and female mice, aged 12–24 weeks at the start of behavioural experiments. The Stanford Administrative Panel on Laboratory Animal Care (APLAC) approved all experiments.

Virus injections. For miniature microscope and brain slice experiments, we used AAV2/9-CAG-FLEX-GCaMP6m-WPRE.SV40 (1.37×10^9 genome copies (GC) μl^{-1}; Penn Vector Core). For two-photon imaging experiments, we used the *Camk2a* promoter to drive GCaMP expression (AAV2/9-CaMKII-GCaMP6m; 1.8×10^9 GC μl^{-1}) in both SPN types. To inject the virus, we anaesthetized mice with isoflurane (2% in O_2) and stereotaxically injected virus into the dorsomedial striatum (anteroposterior (AP): 1.0 mm from bregma; mediolateral (ML): 1.5 mm from midline; dorsoventral (DV): −2.7 mm (down to −3.2 mm then back up to −2.7 mm from dura)). The injection needle had a 33-gauge bevelled tip. We injected 500 nl of virus at a rate of 250 nl min^{-1}. After the injection was done, we waited 10 min and then withdrew the syringe. We recorded the bregma–dura distance for subsequent positioning of the optical guide tube, sutured the scalp, and allowed the mice to recover for a week before implanting the guide tube.

In vitro electrophysiological and Ca^{2+} imaging studies in striatal tissue slices. Using established techniques[39], we performed dual Ca^{2+} imaging and electrophysiological studies of SPN dynamics in live brain slices obtained from *Drd1a*^{cre} and *Adora2a*^{cre} mice >3 weeks after virus injection. The numerical aperture of the imaging system was matched to that of the miniature microscope used in freely behaving mice. We imaged striatal Ca^{2+} transients at a frame acquisition rate of 20 Hz, using a scientific-grade CMOS camera (ORCA-Flash 4.0 LT, Hamamatsu Photonics) and MicroManager software (NIH)[40]. Concurrently, we performed whole-cell current-clamp recordings of SPN activity using a patch pipette (3–5 MΩ) and a Multiclamp 700B (Molecular Devices) patch-clamp amplifier. Additional details can be found in the Supplementary Methods.

Surgeries. To prepare mice undergoing 6-OHDA lesions and imaging, we anaesthetized mice with isoflurane (2% in O_2) and used a 0.5-mm-diameter drill bit to create a craniotomy dorsal to the SNc (AP = −3.5 mm; ML = 1.25 mm) for insertion of a 26-gauge guide cannula (2.5-mm-long projection, Plastics One, Inc.). We drilled three additional small holes (0.5-mm diameter) at spatially distributed locations for insertion of stabilizing skull screws.

We used a 1.4-mm-diameter drill bit to create another craniotomy (AP = 1.0 mm; ML = 1.5 mm) for implantation of the optical guide tube. We fabricated this guide tube by using ultraviolet liquid adhesive (Norland #81) to fix a 2.5-mm-diameter disc of #0 glass to the tip of a 3.8-mm-long, extra-thin 18-gauge stainless steel tube (McMaster-Carr). We ground off any excess glass using a polishing wheel (Ultratec). Using a 27-gauge blunt-end needle, we aspirated the cortex down to DV = −2.1 mm from the dura and implanted the exterior glass face of the optical guide tube at DV = −2.35 mm. We lowered the SNc guide cannula to DV = −1.0 mm from the dura. After stereotaxic placement of these components, we applied Metabond (Parkell) to the skull and fixed the full assembly using dental acrylic (Coltene). After the acrylic hardened, we used a second batch of acrylic to attach an aluminium head bar to the cranium, for the purpose of head-fixing the mice during subsequent experimental procedures. Mice recovered for 3–4 weeks before two-photon imaging experiments or mounting of the miniature microscope.

Mounting of the miniature microscope. At 3–4 weeks after guide tube implantation, we assessed the extent of Ca^{2+} indicator expression in the dorsomedial striatum. To do this, we inserted a gradient refractive index (GRIN) lens (1 mm diameter; 4.12 mm length; 0.46 numerical aperture; 0.45 pitch; GRINTECH GmbH or Inscopix Inc.) into the optical guide tube and used a commercial two-photon fluorescence microscope (Ultima, Bruker) to image the striatum of each mouse while it was anaesthetized with isoflurane (2% in O_2). In mice with uniform indicator expression, we secured the GRIN lens in the guide tube with ultraviolet (UV)-light curable epoxy (Loctite 4305).

After affixing the GRIN lens, we lowered a miniature microscope (nVistaHD, Inscopix Inc.) towards the GRIN lens until the fluorescent tissue was in focus. To secure the miniature microscope to the cranium, we created a base on the cranium around the GRIN lens using blue-light curable resin (Flow-It ALC; Pentron). We attached the base plate of the miniature microscope to the resin base using UV-light curable epoxy (Loctite 4305). After affixing its base plate, we released the microscope and attached a base plate cover (Inscopix Inc.). We coated the resin with black nail polish (Black Onyx, OPI) to make it opaque.

6-OHDA infusions. To block serotonin and noradrenaline transporters and thereby prevent lesioning of non-dopamine monoamine neurons, we injected mice with desipramine (25 mg kg^{-1}; i.p.) 30 min before 6-OHDA infusion[41]. We anaesthetized the mice with isoflurane (2% in O_2) and stereotaxically inserted into the craniotomy above the SNc (see 'Surgeries') an injection cannula (33 gauge, 17-mm-long) that was connected to a syringe pump loaded with 6-OHDA (4 μg μl^{-1} in saline). We sequentially infused 6-OHDA (650 nl at 100 nl min^{-1}) at three sites: DV = −4.2 mm, −4.0 mm and −3.8 mm below the dura. We withdrew the injection cannula 10 min after the final infusion. After infusion, we monitored the body mass of each mouse and subcutaneously administered 1 ml lactated Ringer's solution to prevent dehydration. In the first 3 days after 6-OHDA infusion, we provided the mice with manually crumbled mouse chow, to aid recovery.

Pharmacology. We dissolved the D1R agonist (SKF81297; 1, 3 or 6 mg kg^{-1}), D1R antagonist (SCH23390; 0.2 mg kg^{-1}), D2R agonist (quinpirole; 1, 3 or 6 mg kg^{-1}), D2R antagonist (raclopride; 1 mg kg^{-1}), or L-DOPA (1, 6 or 10 mg kg^{-1}) mixed with benserazide (15 mg kg^{-1}) in 0.9% saline solution (all compounds from Sigma-Aldrich). We delivered all drugs systemically to the mice via intraperitoneal injection (10 ml kg^{-1} injection volume). We selected doses based on published receptor occupancy data in systemically injected rodents[42–44] and our own evaluations of the dose-dependent effects of these drugs on behaviour in hemiparkinsonian mice (Extended Data Fig. 9). Specifically, we aimed to select doses with overlapping ranges of behavioural potency to test during Ca^{2+} imaging (Fig. 4). Note that SCH23390 does bind to 5HT2 receptors, but its receptor occupancy level on 5HT2 receptors is 40–50 times less than that of D1Rs at the dose we used[45,46]. For all Ca^{2+} imaging sessions, we waited 15 min after drug injections before recording neural activity for 30 min. See Extended Data Fig. 9 for the time-dependence of drug efficacy.

Experimental timeline. Before the lesion, we administered mice the D1R antagonist SCH23390 (day −4, 0.2 mg kg^{-1}), the D2R antagonist raclopride (day −3, 1 mg kg^{-1}), the D1R agonist SKF81297 (day −2, 1 mg kg^{-1}), and the D2R agonist quinpirole (day −1, 1 mg kg^{-1}). After the lesion, we administered quinpirole (day 15, 1 mg kg^{-1}; day 16, 6 mg kg^{-1}), SKF81297 (day 17, 1 mg kg^{-1}; day 18, 6 mg kg^{-1}), and the dopamine precursor L-DOPA (day 19, 1 mg kg^{-1}; day 20, 6 mg kg^{-1}; day 21, 10 mg kg^{-1}). On days on which mice received drug treatments, we performed 30 min of Ca^{2+} imaging before administering the drug, and another 30 min of Ca^{2+} imaging afterward.

Ca^{2+} imaging in freely moving mice. Brain imaging in freely moving mice occurred in a circular arena (31 cm in diameter). To habituate mice to this arena, we allowed them to explore it for 1 h on each of three sequential days before any Ca^{2+} imaging. Prior to each imaging session (Fig. 1a), we head-fixed each mouse by its implanted head bar and allowed the mouse to walk or run in place on a running wheel. We then attached the miniature microscope and adjusted the focal setting to optimize the field-of-view, in the first imaging session, or in subsequent sessions to match the field-of-view to that of all prior sessions (Extended Data Fig. 1j).

After securing the microscope to the head of the mouse, we detached the mouse from its head restraint and allowed it to freely explore the circular arena. After allowing ≥10 min for the mouse to habituate to the arena, fluorescence Ca^{2+} imaging commenced using 50–200 μW of illumination power at the specimen plane and a 20-Hz frame acquisition rate. We also acquired 20-Hz movies of the behaviour of each mouse using a TTL-triggered video camera (SVWGAM; EPIX Inc.), a varifocal lens (T3Z2910CS; Computar), an image frame grabber card (PIXCI-SI; EPIX Inc.) and image-acquisition software (XCAP; EPIX Inc.). We concurrently recorded behavioural and Ca^{2+} imaging data in sessions generally lasting 60 min in total. On days on which the mouse received drug treatments (Fig. 1a), we gave the mouse an injection of saline vehicle, waited 5 min, and then performed 30 min of Ca^{2+} imaging. We then administered the drug, waited 15 min for the drug to take effect, and then acquired another 30 min of Ca^{2+} imaging data.

Two-photon Ca^{2+} imaging in behaving mice. We acquired volumetric Ca^{2+} imaging data from four different axial planes in the brains of head-fixed mice free to behave on a running wheel. The mice expressed the red fluorophore tdTomato in dSPNs and GCaMP6m in both SPN types (see 'Mice'). After implantation of an optical guide tube and GRIN microendoscope in the dorsomedial striatum (see 'Surgeries'), we head-fixed the mice beneath the microscope objective lens carrier of a custom-built two-photon microscope[47]. The microscope was equipped with a resonant galvanometer laser-scanning mirror (CRS 8 K, Cambridge Technologies), allowing a 30-Hz frame acquisition rate (512 × 512 pixels) under the control of ScanImage 5.2 software[48] (Vidrio Technologies). Additional details can be found in the Supplementary Methods.

Rotarod assay. Before day −5 (Fig. 1a), we trained mice for 3–4 days on an accelerating rotarod (EzRod; Omnitech) to ensure that they could remain on the rotarod. Each mouse performed three trials per day, with the rod accelerating from 6 to 60 r.p.m. in 3 min. During subsequent rotarod sessions (days −5, 1 and 14), we imaged SPN Ca^{2+} activity as mice walked on the rotarod at a constant speed of 5 r.p.m. for 10 min. After dopamine depletion, we excluded from

analyses of SPN Ca^{2+} activity any mouse that could not stay on the rotarod for the full 10 min of Ca^{2+} imaging.

Turning bias assay. To eliminate any potential effects on mouse turning behaviour from the miniature microscope or its cable, we studied the behaviour of a separate cohort of mice that underwent unilateral dopamine depletion. This allowed us to assay the dose-dependent behavioural effects of the same drugs that we studied with in vivo Ca^{2+} imaging. We manually scored the number of rotations that mice made ipsilateral and contralateral to the right cerebral hemisphere during 1 h recordings of open field locomotion. We computed the rotational bias of each mouse as the difference between the total numbers of rotations in each direction. We then lesioned the right SNc with 6-OHDA and repeated this scoring procedure 1 day and 14 days after the lesion.

We then evaluated the effects of intraperitoneal injections of saline vehicle, quinpirole (1, 3 and 6 mg kg^{-1}), SKF81297 (1, 3 and 6 mg kg^{-1}) and L-DOPA (1, 6 and 10 mg kg^{-1}) during 3 h of locomotion in the open field, on sequential days. We manually scored the rotational bias of each mouse off-line in 20-min time bins (Extended Data Fig. 9a–d).

Dyskinesia assay. In the same mice and behavioural sessions used to quantify the turning bias, we measured the abnormal involuntary movement score (AIMS) for each mouse following established procedures[31]. This score is a well-known metric used to quantify dyskinesia levels in parkinsonian mice in response to a range of drug treatments and experimental manipulations[31]. In brief, for a period of 3 h after systemic drug injection, every 20 min we assigned each mouse an AIMS value by observing the behaviour of the mouse for a sample period of 60 s. We monitored the mouse for the presence of abnormal (i) axial, (ii) limb and (iii) orofacial movements. To provide multiple viewing perspectives of the mouse during AIMS scoring, we placed a pair of rectangular mirrors (30.5 cm × 45.7 cm) outside the open field arena, at 90° to each other, behind the mouse and opposite to the experimenter. During each 60-s sample period, we assigned the mouse a score of 0–4 in each category (i–iii). A score of '0' signified no observed abnormalities. A score of '1' or '2' signified abnormal behaviour that respectively lasted $<$30 s or $>$30 s. A '3' signified abnormal behaviour that lasted 60 s but that could be interrupted by an external stimulus (for example, a loud clap). A '4' indicated abnormal behaviour that lasted 60 s and could not be interrupted. For each 60-s sample period, we summed the individual category AIMS values to attain the total AIMS value.

Histology. After all behavioural and Ca^{2+} imaging experiments, we euthanized and intracardially perfused the mice with phosphate-buffered saline (PBS) and then a 4% solution of paraformaldehyde in PBS. We sliced the fixed brain tissue using a vibratome (Leica VT1000s) to obtain 80-μm-thick coronal sections. We immunostained the tissue sections with antibodies against tyrosine hydroxylase (1:500, Aves TYH) and GFP (1:1,000, Molecular Probes A-11122) and then applied fluorophore-conjugated secondary antibodies (Jackson Immunoresearch 703-586-155 and 711-546-152, respectively). We visualized immunofluorescence in our sections using a slide-scanning microscope (Olympus VS-120) and confirmed that all mice included for post-lesion analyses had a complete unilateral loss of dopamine neurons in the SNc.

Video analysis of mouse behaviour. We used custom software written in MATLAB to analyse the videos (20-Hz frame acquisition rate) of mouse behaviour acquired during Ca^{2+} imaging with the miniature microscope. First, we ranked all the pixels in each video frame according to their intensity values. Under the lighting conditions used to acquire the videos, the mouse appeared much darker than the surrounding open field arena (Supplementary Videos 1, 2). Therefore, we next determined the centroid location of the mouse in each frame as the mean location of the 1,500 darkest pixels. By visual inspection of each movie, we confirmed that this approach reliably tracked the movements of each mouse and yielded an accurate record of its position. To match the temporal resolution of our down-sampled Ca^{2+} recordings, we down-sampled the locomotor speed traces to 5 Hz via linear interpolation. We classified each 200-ms time bin as one in which the mouse was either 'resting' or 'moving', according to the down-sampled speed trace and using a threshold value of 0.5 cm s^{-1} to separate the two states. If the mouse was 'moving' in two time bins separated by $<$1 s, we classified the intervening time bins as ones in which the mouse was 'moving'.

We applied these analytic procedures uniformly to the behavioural videos across all experimental and drug treatment conditions. Under dyskinetic conditions, mice commonly exhibit ongoing movements of the face, limbs and trunk. In general, these movements did not translate the body centroid sufficiently rapidly to register as locomotor episodes. Nevertheless, an important caveat is that under dyskinetic conditions a greater number of sub-threshold movements may have occurred during the computationally identified 'resting' periods than under normal or parkinsonian conditions.

Classification of movement types. To study and compare movements of different types made by freely moving mice (Extended Data Figs. 3, 8), we used custom software written in MATLAB (Mathworks) to extract from the behavioural videos the intervals from –4 to 4 s surrounding the onset of each movement bout. Using this software, we visually scored each movement bout as an instance of forward locomotion, a left or right turn, grooming, or upward rearing. Additional details are shown in Extended Data Fig. 3.

Quantification of movement in head-restrained mice. To analyse the locomotor behaviour of mice during two-photon Ca^{2+} imaging sessions (see 'Two-photon Ca^{2+} imaging in behaving mice'; Extended Data Fig. 4), we computed the running speed of the mouse using the signals from a rotary encoder on the running wheel and identified movement periods during which the running speed was above a minimum threshold. Additional details are shown in Extended Data Fig. 4.

Basic processing of in vivo fluorescence Ca^{2+} movies. To reduce processing times, we spatially down-sampled the raw Ca^{2+} videos from the miniature microscope using 4 × 4 bi-linear interpolation. To correct images for lateral motions of the brain, we used the image-alignment algorithm, TurboReg[49], to perform a rigid image registration across all frames of the movie. To correct for fluctuations in background fluorescence intensity, we applied a Gaussian low-pass filter to each image, which smoothed all structures $<$100 μm in size, and then divided each image frame by its low-pass filtered version. Using the resultant normalized movie ($F(t)$), we subtracted the time-averaged, mean fluorescence intensity (F_0) of each pixel to obtain the difference movie, $\Delta F(t) = F(t) - F_0$. We then divided this difference by F_0 to obtain movies of relative fluorescence changes, $\Delta F(t)/F_0$. Finally, we temporally down-sampled (4×) the $\Delta F(t)/F_0$ movies to a 5-Hz frame rate via a linear interpolation, and we used the resulting videos for extraction of individual neurons and their Ca^{2+} activity traces.

We processed the raw two-photon Ca^{2+} videos with the same procedures, but with two exceptions: we did not down-sample the movies in space or time, and we applied a median spatial filter (6 × 6 pixels) to the two-photon $\Delta F(t)/F_0$ movies before proceeding to cell sorting. For display purposes only (Supplementary Video 3), we converted the fluorescence trace, $F(t)$, of each pixel into a trace of z scores, $\Delta F(t)/\sigma$. Here $\Delta F(t) = F(t) - F_0$ denotes the deviation of each pixel from its mean value, F_0, and σ denotes the background noise of each pixel, which we estimated by taking the standard deviation values calculated with a sliding 250-s window.

Identification of individual neurons. We identified individual cell bodies in the brain imaging videos by applying to the pre-processed one- and two-photon $\Delta F(t)/F_0$ movies an established algorithm for cell sorting based on principal component and independent component analyses (PCA–ICA)[50]. As in previous work[50], the extracted spatial filters generally had sizes, morphologies and corresponding Ca^{2+} activity traces that were characteristic of individual neurons, but there were also some filters that were obviously not neurons that we discarded. We verified every cell included in the analyses by visual inspection. We did not register individual cells over multiple days; hence all analyses characterizing the rates, amplitudes and durations of Ca^{2+} events (Extended Data Fig. 1l–n) were conducted separately for each day of experimentation, over the uniform imaging duration (1 h per session).

Cells identified in the two-photon Ca^{2+} videos underwent further analyses, to classify each cell as being either an iSPN or dSPN, and to remove duplicate copies of individual cells found in more than one image plane. We first manually identified the centroids of all visible cells in each plane labelled with tdTomato. We then compared these centroid locations to those of the cells extracted from the two-photon Ca^{2+} videos and matched each tdTomato-expressing cell to the nearest unassigned cell in the Ca^{2+} video (Extended Data Fig. 4b, c).

To remove duplicate copies of individual cells seen on more than one plane of the two-photon Ca^{2+} videos, we computed for all nearby cells found on different planes both the distance between the centroids of the two cells and the Pearson correlation coefficient of their $\Delta F(t)/F_0$ activity traces. We identified duplicate copies of the same cell as cell pairs within 15 μm of each other and with an activity correlation coefficient $>$0.7. Among the duplicates, we retained the one with the Ca^{2+} activity trace with the highest signal-to-noise ratio.

Detection of Ca^{2+} transients. After identifying individual cells in the one- and two-photon brain imaging datasets, we detected Ca^{2+} events in the fluorescence trace of Ca^{2+} activity of each cell using a threshold-crossing algorithm to detect fluorescence peaks that were $\geq$3 s.d. above the baseline signal value for $\geq$1.4 s. We determined the time of each Ca^{2+} event as the temporal midpoint between the time of the Ca^{2+} event's fluorescence peak and the most recent preceding trough in fluorescence[23].

On 6.4 ± 3% (mean ± s.d.) of all detected Ca^{2+} events in the one-photon datasets, bright fluorescence increases from a Ca^{2+} event in one cell occupied more pixels than a single spatial filter. To prevent contamination of the time traces of other cells we took a conservative approach and allowed only a single cell among a group of neighbours to register a Ca^{2+} event in a single 200-ms time frame. We defined neighbours as cells that had centroids within 20 μm of one another[23]. If multiple Ca^{2+} events arose within 200 ms in neighbouring cells, we retained only the transient with the greatest peak value.

To characterize the waveforms of the Ca^{2+} transients of the cells (Extended Data Figs. 1l–n, 5f–h), we took the spatial filter of each cell, zeroed all pixels with values <50% of the peak value, and applied the truncated filter to the movie of $\Delta F(t)/F_0$ to generate a time trace of Ca^{2+} activity (Fig. 1d). Using the previously identified Ca^{2+} events, we then considered the statistical distribution of Ca^{2+} transient waveforms among all events and SPNs of a given type. From this distribution, we computed the median and interquartile range values of Ca^{2+} transient amplitude and duration (Extended Data Fig. 1l–n). With the exception of these basic characterizations of the Ca^{2+} transient waveforms, all subsequent analyses made use only of the occurrence times of the Ca^{2+} transients and treated these occurrences as binary events.

Determinations of coactivity levels in cell pairs. SPN ensembles displayed prominent temporal correlations between cells across timescales of ~1–2 s (Supplementary Videos 1–4). To characterize correlations at these timescales, we first applied a 'forward-smoothing' by taking the binarized traces of Ca^{2+} events of individual cells and extending the number of time bins (200 ms per bin after temporal down-sampling; see 'Basic processing of in vivo fluorescence Ca^{2+} movies') in which a cell was marked as active so as to include all frames within 1 s after the Ca^{2+} event. Then, to assess the extent to which pairs of cells had correlated patterns of activity, for each cell pair we computed the Jaccard index characterizing the similarity between the binarized Ca^{2+} activity traces of two cells. We used this index as a metric of pairwise coactivation and determined it as the total number of time bins during which both cells in a pair were active, divided by the total number of time bins in which either cell was active. We chose the Jaccard index because, unlike more common measures of correlation, such as the Pearson correlation coefficient, the Jaccard index does not depend on the number of time bins in which neither cell is active and in this sense is more sensitive to the periods of joint activity rather than those of joint inactivity. We computed the mean value of the Jaccard index as a function of the distance between the cells in a pair (Fig. 2d and Extended Data Figs. 4j, 6e).

To control for changes in pairwise coactivation that might be simply owing to the changes in Ca^{2+} event rates resulting from the experimental manipulations and drug treatments, we also computed the Jaccard index for shuffled datasets in which the Ca^{2+} events of each cell were randomly re-distributed in time. We performed 1,000 independent shuffles of the Ca^{2+} event times for each cell, when mice were resting or in locomotion. To compare pairwise coactivation levels in the real data against those in the shuffled data, we normalized the plots of mean Jaccard index for the real data by the corresponding values for the shuffled data (Fig. 2d, e and Extended Data Figs. 4j, k, 6e). Alternatively, we subtracted the coactivity values determined from the shuffled datasets from those of the real data, and compared the resultant values across different experimental conditions for the proximal cell pairs (cell centroid separations between 20–100 μm lateral separation) (Figs. 3j, 4f, 5g and Extended Data Fig. 7i, j).

We also checked whether SPN activity rates varied across the imaging field-of-view and thus affected estimates of coactivity levels. We computed the Pearson correlation coefficient between the Ca^{2+} event rate of every cell and its distance from the centre of the field-of-view. We found a very weak but statistically significant correlation between these two variables ($r = 0.07 \pm 0.02$; $P < 10^{-10}$; $n = 29{,}097$ cells; $n = 19$ mice, each sampled during five imaging sessions), which explained almost none of the variations in the Ca^{2+} activity rates of the cells across the SPN population ($R^2 = 0.005$). Overall, effects arising from the locations of the cells in the field-of-view were far too weak to account for the substantial distance-dependence of pairwise coactivity levels of the cells (Fig. 2d).

We determined pairwise coactivity levels in the two-photon Ca^{2+} videos using identical procedures as for the one-photon Ca^{2+} videos.

Spatial coordination index. In the Ca^{2+} videos, there were plainly evident, spatially correlated patterns of SPN activation at the seconds time scale. To characterize the spatial structure of these patterns at individual time points in the videos, we computed an index of spatial coordination. To calculate how this index varied over an entire imaging session (Extended Data Fig. 2), we took the binarized traces of the Ca^{2+} events of individual cells and extended the number of time bins (200 ms each after temporal down-sampling; see 'Determinations of coactivity levels in cell pairs') in which a cell was marked as active so as to include all frames within 1 s after each Ca^{2+} event. We performed this temporal expansion, which increased the time window over which cells appeared as jointly active, to highlight the spatially clustered activation of cells at the seconds time scale. For each time bin, we then computed the set of distances between all pairs of cells that were active in the time bin. For each time bin, we also calculated this set of pairwise distances for shuffled versions of the data, in which we randomized the identities of the active cells while maintaining their centroid coordinates as well as the same number of active cells in the time bin. We performed 1,000 independent shuffles for each time bin. Aggregating the results across all 1,000 shuffles, we computed the cumulative distribution function of pairwise distances between active cells. For each time bin, we also computed this cumulative distribution function for the real data, and performed a pair of one-tailed Kolmogorov–Smirnov tests that compared the cumulative distribution functions of pairwise distances in the shuffled and real versions of the data. With one of the two tests, we examined the hypothesis that the active cells in the real data were distributed closer together than expected by chance, and with the other, we examined the hypothesis that the active cells in the real data were distributed further away from each other than expected by chance. We took the logarithm (base ten) of the lesser of the two P values (that is, the P value from the test that more significantly rejected its null hypothesis). We multiplied the resultant number by negative one or one, respectively, according to whether the locations of the active cells in the time bin were spatially correlated or anti-correlated (as determined by which of the two Kolmogorov–Smirnov tests gave the more significant result). We assigned the spatial coordination index (SCI) the value of the resulting product.

To characterize the time-dependent relationship between mouse speed and the SCI, we computed the time-dependent cross-correlation function between the two variables (Extended Data Fig. 2e, f). To analyse the effects of the temporal sampling rate on these calculations, before computing the SCI, we first forward-smoothed (see previous paragraph) the Ca^{2+} event rasters using a variety of different smoothing time constants from 200 to 1,000 ms. After computing the speed-SCI cross-correlation function, we normalized it to the mean of its values between the intervals from −4 to −3 s and from 3 to 4 s.

Analyses of Ca^{2+} event rates as a function of locomotor speed. To examine how the rate of Ca^{2+} events varied with changes in locomotor speed (Figs. 2a, 3e, 4b–d, 5c and Extended Data Figs. 4g, 7d, e), we sorted the individual image frames of the behaviour video of each mouse according to the instantaneous locomotor speed of the mouse. We then binned the image frames into sets of images for which the locomotor speed was the same to within 0.036–0.73 cm s^{-1}, using finer bins at lower speeds and coarser bins at higher speeds. For each image set, we computed its mean rate of Ca^{2+} events across all detected SPNs.

To make comparisons between mice (Fig. 2a), we took the mean Ca^{2+} event rate of each mouse as a function of locomotor speed and normalized this curve to the mean Ca^{2+} event rate of each mouse while it was at rest (speed <0.5 cm s^{-1}). We averaged these normalized traces across the set of all *Drd1a*^{cre} or *Adora2a*^{cre} mice.

To compare Ca^{2+} event rates during the various drug treatments to those following injections of saline vehicle (Figs. 4b–d, 5c and Extended Data Fig. 7d, e), we normalized the Ca^{2+} event rates for each mouse and each drug condition by the mean rate when the mouse was at rest after having been given saline vehicle. For each drug condition, we then averaged these normalized curves across all mice in the cohort.

To compare Ca^{2+} event rates before and after dopamine depletion (Fig. 3e), we first computed the curve of the mean Ca^{2+} event rate of each mouse as a function of locomotor speed. We averaged these curves across mice of a given genotype, and then normalized the resulting trace to the mean rate when the mice were at rest in baseline recordings, before 6-OHDA lesion. For all comparisons, we calculated the s.e.m. for the mean Ca^{2+} event rate for each mouse and speed bin.

Determinations of motion onset- and offset-triggered averages. We identified onsets of locomotion by finding all movement bouts (≥2 s in duration) that occurred ≥2 s after the prior movement bout. We identified offsets of locomotion by finding all movement bouts that preceded the next movement bout by ≥2 s. To calculate motion onset- or offset-triggered averages, for each mouse we first normalized the speed-dependent, mean rates of Ca^{2+} events or mean spatial coordination indices to the corresponding mean values from when each mouse was at rest during the period of −2 to −1 s relative to motion onset. We then took all motion onset and offset occurrences and calculated the time-dependent, onset- and offset-triggered averaged traces of the normalized Ca^{2+} event rate or spatial coordination index. We averaged these traces across all mice in each cohort.

To calculate the average times at which dSPN and iSPN activity reached their half-maximum values relative to the onset of movement, we fit logistic curves to the mean trace of the Ca^{2+} event rate of each mouse for the interval of −2 to 2 s relative to movement onset. We then determined the half-maximum activation time from the fit parameters. We averaged these time values over all mice of the same genotype.

To calculate the average times at which dSPN and iSPN activity commenced relative to the onsets of locomotion on the running wheel (Extended Data Fig. 4h), we calculated the percentage of cells of each type that were active in each time bin in the binarized traces of Ca^{2+} activity (see 'Detection of Ca^{2+} transients'). Across all instances of motion onset, we computed the average number of dSPNs and iSPNs that were active in each time bin over the interval of −3 to 1 s relative to motion onset. We then fit these averaged traces to a logistic curve. From each parameterized fit curve, we determined the onset time as the time at which the mean percentage of active cells was ≥3 s.d. of the percentage of active cells during the baseline periods of −3 to −1 s relative to motion onset.

Analysis of Ca^{2+} event-triggered averages. To examine how the occurrences of the Ca^{2+} events of cells (in the one- or two-photon imaging datasets) correlated in

time with changes in the locomotor speed of the mice (Figs. 2b, 3h and Extended Data Fig. 4i), we computed the time trace of the Ca^{2+} event-triggered, mean locomotor speed for each cell. For each mouse, we averaged these event-triggered traces of mean speed across all cells and normalized the resulting trace by its value at either −2 s or −20 s relative to Ca^{2+} event onset, in the one- and two-photon imaging studies, respectively. In experiments with freely moving mice, we averaged these traces across all mice with the same genotype. In dual-colour imaging experiments with head-fixed mice, we averaged the traces across all SPNs of the same type. We computed the first temporal moment of the resulting averaged trace across the interval of −2 to 2 s, to determine the temporal offset between peak locomotor speed and the occurrence of an SPN Ca^{2+} event.

Similarities of the neural ensembles activated by movements of different types. To statistically evaluate the relative similarity of the neural ensembles activated during movement bouts of the same or different types, and during baseline periods, we used the Jaccard similarity index (Extended Data Figs. 3d, e, 8d–g). Additional details can be found in the Supplementary Methods.

Decoding mouse locomotor speed based on SPN Ca^{2+} activity. We used a generalized linear model (GLM) to make time-dependent predictions of the locomotor speeds of mice based on the $\Delta F(t)/F_0$ activity traces of the cells as determined by two-photon Ca^{2+} imaging. Additional details are shown in Extended Data Fig. 4.

Computational simulations of SPN activity traces. To examine the temporal accuracy with which we could use Ca^{2+} events in SPNs to determine the times of the accompanying action potentials, we created and analysed artificial datasets based on the fluorescence responses to action potentials observed in our dual electrical–optical recordings in vitro and on basic facets of the fluorescence recordings in vivo. Additional details can be found in the Supplementary Methods.

Data analyses and statistical tests. We performed data analysis using custom software written in MATLAB and ImageJ. We also used the Prism (Graphpad) and R programming environments for statistical analyses. We used two-tailed, non-parametric statistical tests to avoid assumptions of normal distributions and equal variance across groups. All signed-rank tests were Wilcoxon signed-rank tests. All rank-sum tests were Wilcoxon rank-sum tests. Analyses were performed unblinded. The sizes of our mice samples were chosen to approximately match those of previous work, as there was no pre-specified effect size. In all box-and-whisker plots, horizontal lines denote median values, boxes cover the middle two quartiles, and whiskers span 1.5× the interquartile range. *P* and *n* values for the statistical tests performed in all the figures can be found in the Supplementary Information.

Reporting summary. Further information on experimental design is available in the Nature Research Reporting Summary linked to this paper.

Code availability. The algorithm used for image registration is available on its author's website[49]. The algorithm used for cell sorting is available as Supplementary Material published elsewhere[50]. Other software code that support the findings of this study are available from the corresponding authors upon reasonable request.

Data availability. The data that support the findings of this study are available from the corresponding authors upon reasonable request.

39. Wu, Y. W. et al. Input- and cell-type-specific endocannabinoid-dependent LTD in the striatum. *Cell Rep.* **10**, 75–87 (2015).
40. Edelstein, A. D. et al. Advanced methods of microscope control using μManager software. *J. Biol. Methods* **1**, e10 (2014).
41. Breese, G. R. & Traylor, T. D. Depletion of brain noradrenaline and dopamine by 6-hydroxydopamine. *Br. J. Pharmacol.* **42**, 88–99 (1971).
42. Peng, T. et al. D_2 receptor occupancy in conscious rat brain is not significantly distinguished with [^{3}H]-MNPA, [^{3}H]-(+)-PHNO, and [^{3}H]-raclopride. *Synapse* **64**, 624–633 (2010).
43. Neisewander, J. L., Fuchs, R. A., O'Dell, L. E. & Khroyan, T. V. Effects of SCH-23390 on dopamine D_1 receptor occupancy and locomotion produced by intraaccumbens cocaine infusion. *Synapse* **30**, 194–204 (1998).
44. Wadenberg, M. L., Kapur, S., Soliman, A., Jones, C. & Vaccarino, F. Dopamine D_2 receptor occupancy predicts catalepsy and the suppression of conditioned avoidance response behavior in rats. *Psychopharmacology* **150**, 422–429 (2000).
45. Riddall, D. R. A comparison of the selectivities of SCH 23390 with BW737C89 for D_1, D_2 and 5-HT_2 binding sites both in vitro and in vivo. *Eur. J. Pharmacol.* **210**, 279–284 (1992).
46. Suhara, T. et al. D_1 dopamine receptor binding in mood disorders measured by positron emission tomography. *Psychopharmacology* **106**, 14–18 (1992).
47. Lecoq, J. et al. Visualizing mammalian brain area interactions by dual-axis two-photon calcium imaging. *Nat. Neurosci.* **17**, 1825–1829 (2014).
48. Pologruto, T. A., Sabatini, B. L. & Svoboda, K. ScanImage: flexible software for operating laser scanning microscopes. *Biomed. Eng. Online* **2**, 13 (2003).
49. Thévenaz, P., Ruttimann, U. E. & Unser, M. A pyramid approach to subpixel registration based on intensity. *IEEE Trans. Image Process.* **7**, 27–41 (1998).
50. Mukamel, E. A., Nimmerjahn, A. & Schnitzer, M. J. Automated analysis of cellular signals from large-scale calcium imaging data. *Neuron* **63**, 747–760 (2009).

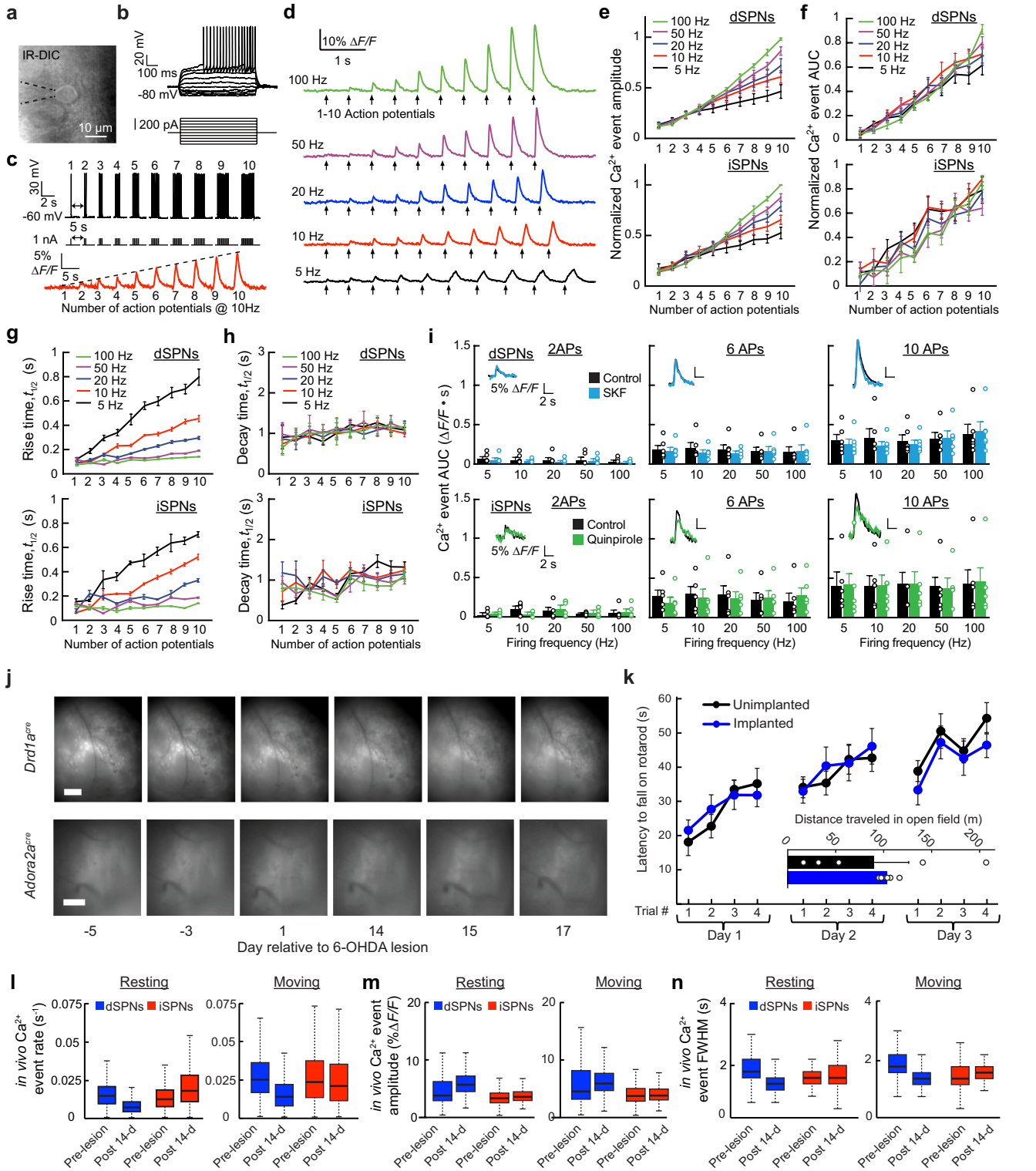

Extended Data Fig. 1 | See next page for caption.

Extended Data Fig. 1 | Characterizations of striatal SPN Ca^{2+} activity patterns in live brain slices and recorded in behaving mice using a chronic microendoscopy preparation. a, We performed whole-cell patch-clamp recordings of SPNs in acute brain slices, using dual epifluorescence and infrared Nomarski (IR-DIC) microscopy to guide the recordings. We selectively recorded from fluorescent dSPNs and iSPNs in brain slices from *Drd1a*^{cre} and *Adora2a*^{cre} mice that had been injected into the striatum with AAV2/9-CAG-FLEX-GCaMP6m-WPRE.SV40. The numerical aperture used for the fluorescence recordings was matched to that used for Ca^{2+} imaging studies in freely behaving mice (Methods). **b**, Illustrative traces (top) of neural membrane potential (V_m) showing the changes that result upon stepwise injections of electrical current (bottom). The traces exhibit typical waveforms for SPNs. **c**, To visualize Ca^{2+} transients evoked by different numbers and frequencies of action potentials in iSPNs and dSPNs in brain slice recordings, we elicited spiking with 1-nA pulses (1-ms duration; 1 to 10 pulses, delivered at 5, 10, 20, 50 and 100 Hz). Top, an example of a V_m trace during 1–10 pulses injected at 10 Hz. Middle, example traces of current pulse injections delivered at 10 Hz. Bottom, a representative trace of somatic Ca^{2+} transients in response to the same 10-Hz current injections. **d**, Example Ca^{2+} activity traces for each current injection pattern tested in brain slices. As expected, electrical stimulation at higher frequencies evoked larger amplitude Ca^{2+} transients, with more sharply rising Ca^{2+} waveforms than those evoked at lower stimulation frequencies. Arrows mark current injections. **e**, **f**, Mean ± s.e.m. values for Ca^{2+} transient amplitudes (**e**) and area under the Ca^{2+} transient waveform (AUC; **f**) as a function of the number of action potentials evoked, for dSPNs and iSPNs in brain slices. Values for each cell are normalized to those evoked at the highest stimulation intensity (10 action potentials, 100 Hz). Ca^{2+} event amplitudes rose linearly with the number of action potentials ($R^2 > 0.99$ for 5–20 Hz; $R^2 > 0.97$ for all frequencies). There were no significant differences in event amplitude or AUC between dSPNs and iSPNs, at any stimulus intensity. $n = 9$ dSPNs and 8 iSPNs; two-way, mixed-design ANOVA. Exact *P* values can be found in the Supplementary Information for all extended data figures. **g**, **h**, Mean ± s.e.m. values for half-rise (**g**) and half-decay (**h**) times ($t_{1/2}$), measured for the Ca^{2+} events evoked in dSPNs and iSPNs in brain slices, plotted as a function of the number of action potentials. Consistent with their more prolonged stimulus durations, lower stimulation frequencies yielded greater increases in the transient rise time. Ca^{2+} transient decay times were nearly independent of action potential frequency or number. **i**, Mean ± s.e.m. values of the AUC of stimulus-evoked Ca^{2+} events in dSPNs and iSPNs in brain slices, under control conditions or perfused with SKF81297 (1 μM) or quinpirole (10 μM), respectively. Neither drug significantly affected somatic Ca^{2+} event AUCs in either SPN type, regardless of stimulus intensity. $n = 6$ dSPNs and 6 iSPNs; two-way, repeated-measures ANOVA. The individual data points are plotted alongside the mean values. **j**, Two example time-lapse fluorescence image series, acquired over the course of experiments in a *Drd1a*^{cre} mouse (top) and an *Adora2a*^{cre} mouse (bottom). Scale bars are 125 μm and apply uniformly to all panels within each row. Insets show example Ca^{2+} transients in the absence and presence of dopamine receptor agonist SKF81297 or quinpirole. Scale bars are uniformly sized for all insets. **k**, Surgical implantation of the microendoscope did not affect the ability of mice to improve their motor performance on the accelerating rotarod assay, as shown by their increased latencies to fall off the rod, which parallel the performance improvements of control mice without an implanted microendoscope. $P = 0.8$; two-way, repeated-measures ANOVA; $n = 13$ control and 20 implanted mice. Inset, Microendoscope implantation did not alter levels of spontaneous movement in an open field arena. $P = 0.7$; $n = 5$ control and 6 implanted mice; Wilcoxon rank-sum test. Data points from individual mice are shown as open circles. **l**–**n**, Box-and-whisker plots of the rates (**l**), amplitudes (**m**) and full-width at half-maximum (FWHM) durations (**n**) of Ca^{2+} events observed in live normal (untreated) mice in individual dSPNs and iSPNs, before (Pre-lesion) and after (Post 14-d) dopaminergic lesions, as the mice were resting (left) or moving (right). In resting mice, Ca^{2+} event rates decreased in dSPNs and increased in iSPNs after the lesion (**l**) as characterized in Fig. 3. When the mice were moving, Ca^{2+} event rates in iSPNs were similar before and >14 days after the lesion, whereas the rates in dSPNs were depressed after the lesion. Each box-and-whisker plot is based on $n = 3{,}325$–$3{,}703$ dSPNs or iSPNs, from 12 *Drd1a*^{cre} and 13 *Adora2a*^{cre} mice, respectively, tracked before or 14 days after the 6-OHDA lesion. Horizontal lines denote median values, boxes cover the middle two quartiles and whiskers span 1.5× the interquartile range. Data denoted as 'Pre-lesion' were taken on day −5. Data denoted as 'Post 14-d' were taken on day 14.

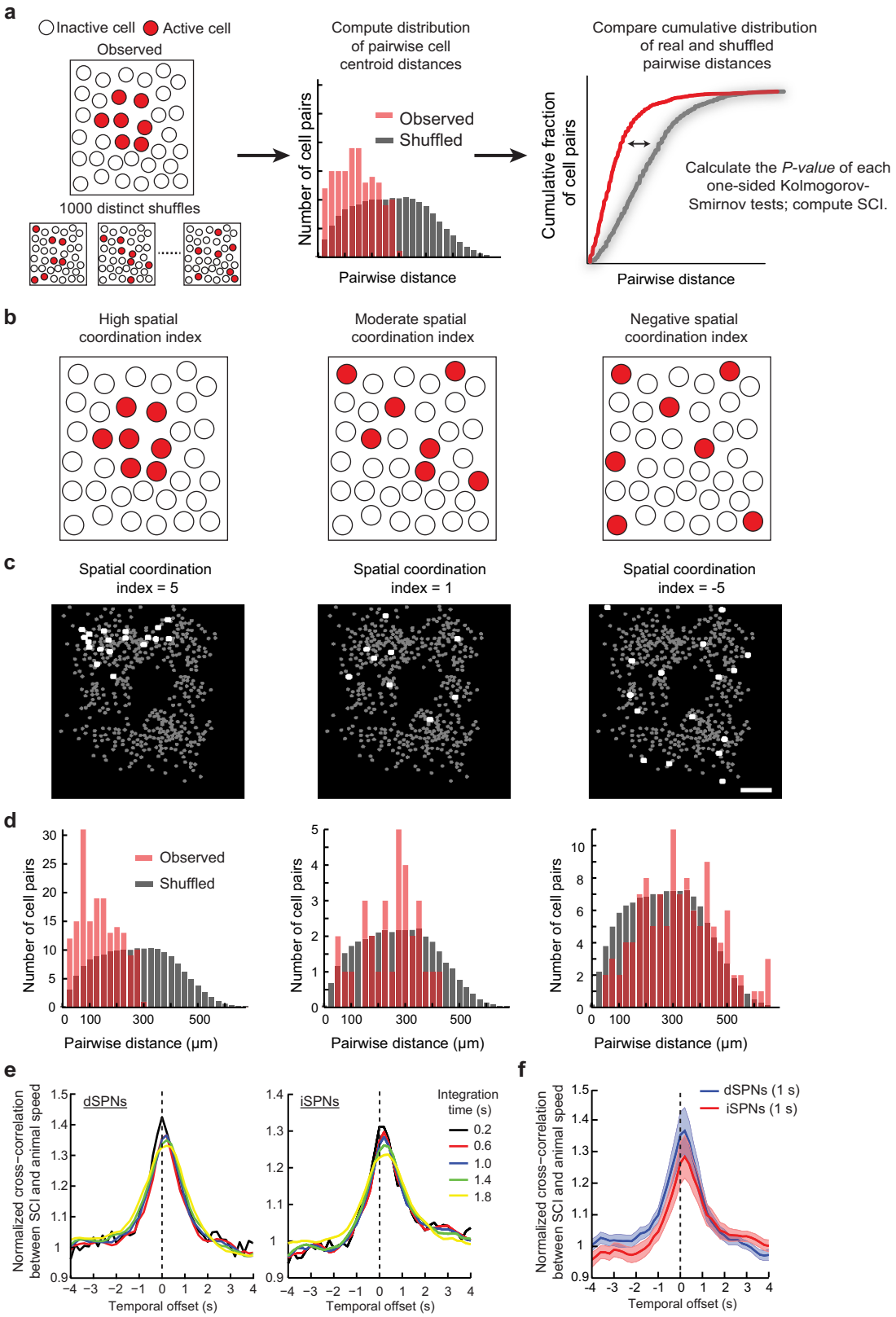

Extended Data Fig. 2 | See next page for caption.

Extended Data Fig. 2 | The spatial coordination index is a metric of the extent to which the activated neurons at an individual time point are spatially clustered. a, Outline of the algorithm (Methods) used to compute the SCI at individual time points in the fluorescence Ca^{2+} movies. For each time point in a $\Delta F(t)/F_0$ movie, we created an image of all cells that were coactive within 1 s of each other. A schematic of an example image (left) has a mixture of active (red) and inactive (white) cells. We computed the set of distances between all pairs of active cells in the image (middle). We then compared these values to the set of pairwise distances between active neurons in shuffled versions of the data from the same image, in which the identities of all the individual cells were randomly permuted while maintaining the same set of cell centroid locations. The shuffled dataset as a whole comprised 1,000 different random shuffles. We compared the cumulative probability distribution function (CDF) of all pairwise distances between active cells in the real image, to that for the shuffled data (right). We then tested two hypotheses, that the activated cells in the real image were either more spatially clustered than expected from a random pattern of activation, or less spatially clustered than expected from random activation. To test these two hypotheses, we performed a pair of one-sided Kolmogorov–Smirnov tests, comparing the real CDF values to those of the shuffled data. We determined the SCI by selecting the smaller of the two *P* values from these two tests, taking its logarithm, and assigning the sign of the index according to whether the CDF of the real data showed greater (positive sign) or less (negative sign) spatial clustering than the CDF of the shuffled data. **b**, Depictions of three images with different SCI values. The left image has an SCI >0, due to its many neighbouring coactive cells. The middle image has an SCI near zero, implying the activation pattern is consistent with that of a random distribution. The right frame has an SCI <0, indicating the active cells are further apart than generally expected of random activity. **c**, Examples of three image frames of different SCI values, from an actual Ca^{2+} movie acquired in a *Drd1a*^{cre} mouse. Active cells are shown enlarged and shaded white, whereas inactive cells are shaded grey. On the left is an image with multiple neighbouring coactive neurons and a high SCI. The middle image has a modest but positive SCI. The right image has a negative SCI, indicating that the activated cells are further apart than expected given a random pattern of activation. **d**, Distributions of pairwise distances between all pairs of active dSPNs for the three corresponding image frames shown in c. The distributions for the real data are shown in red, whereas those for the shuffled datasets are shown in grey. **e**, Mean time-dependent cross-correlation functions between mouse speed and the SCI of Ca^{2+} activity in dSPNs (left) and iSPNs (right). Cross-correlation values are shown normalized to their values for abscissa values of ± 4 s (Methods). We computed the SCI from Ca^{2+} event traces to which we applied forward-smoothing, using one of five different filter values (coloured curves; Methods). Error bars are omitted for clarity in **e**, but are comparable to those shown in **f**. The centre-of-mass of the cross-correlation functions occurred at positive time lags (around 12–60 ms), indicating that rises in spatially coordinated Ca^{2+} activity preceded increases in mouse speed ($P < 0.06$ for both genotypes and all filter time constants; Wilcoxon signed-rank test), but there were no significant differences across the two mouse lines ($P > 0.05$ for all filter time constants; Wilcoxon rank-sum test; $n = 37$ cross-correlation functions from 16 *Drd1a*^{cre} mice and $n = 52$ from 21 *Adora2a*^{cre} mice). **f**, Mean cross-correlation functions between mouse speed and the SCI of Ca^{2+} activity in dSPNs and iSPNs computed from Ca^{2+} event rasters forward-smoothed with a 1,000-ms time constant. Shading indicates s.e.m. **e**, **f**, Values taken from $n = 16$ *Drd1a*^{cre} mice and $n = 21$ *Adora2a*^{cre} mice, aggregated over the 1-h recordings on day -5 and the 30-min recordings performed on days -4 to -1 after saline vehicle injection but before drug administration.

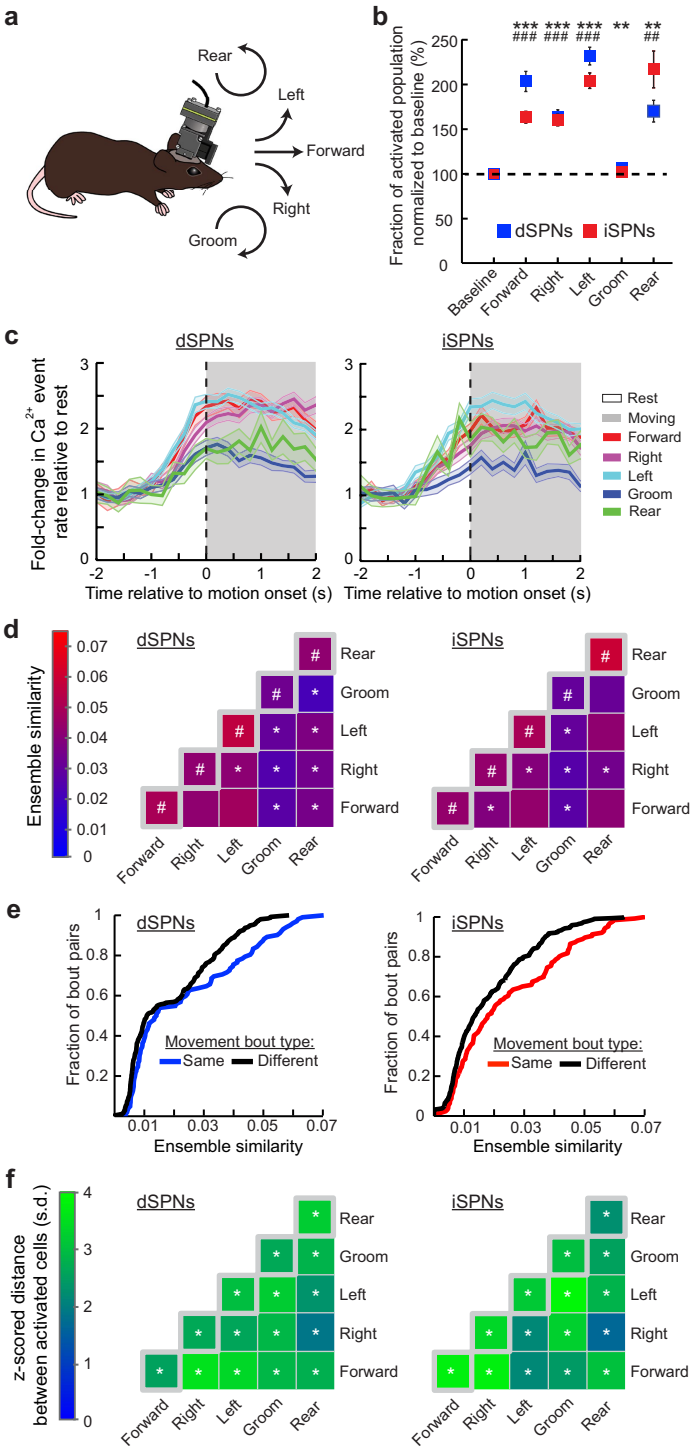

Extended Data Fig. 3 | See next page for caption.

Extended Data Fig. 3 | Different types of movements recruit distinct but overlapping populations of spatially proximal dSPNs and iSPNs. **a**, To study and compare movements of different types made by freely moving mice, we used custom software to extract from the behavioural videos the intervals from −4 to 4 s surrounding the onset of each movement bout. Using this software, we manually labelled each bout as an instance of forward locomotion, a left or right turn, grooming or upward rearing. If the mouse made multiple types of movement within an individual bout, we labelled the bout according to the first movement type exhibited, as only the interval from −1 to 2 s relative to motion onset was used in subsequent analyses of the accompanying neural Ca^{2+} activity. **b**, The fraction (mean ± s.e.m.) of SPNs that exhibited Ca^{2+} activity, relative to the baseline periods immediately preceding each movement type. Relative to baseline (dashed line), there was a significant increase in the fraction of dSPNs and iSPNs activated for all movement types except grooming. $^{**}P < 5 \times 10^{-3}$ and $^{***}P < 5 \times 10^{-8}$ for dSPNs; $^{\#\#}P < 10^{-4}$ and $^{\#\#\#}P < 10^{-10}$ for iSPNs; Wilcoxon signed-rank test. Data in **b** and **c** are from $n = 492$ forward movements, 657 right turns, 810 left turns, 732 grooming and 204 rearing bouts from 17 *Drd1a*^{cre} mice, and $n = 790$ forward, 785 right turns, 1,015 left turns, 792 grooming and 164 rearing bouts from 21 *Adora2a*^{cre} mice. **c**, Rates (mean ± s.e.m.) of Ca^{2+} events in dSPNs and iSPNs, plotted as a function of time relative to the onsets of different types of movements. Event rates are shown normalized to the values of −2 to −1 s before motion onset and rose significantly above baseline values during all types of movement in both cell types. $P < 10^{-6}$ for both cell types and all movement types; Wilcoxon signed-rank test. **d**, Mean values of the neural ensemble similarity computed for the sets of dSPNs and iSPNs that were active during pairs of bouts of either the same (on-diagonal) or different (off-diagonal) types of movements (Methods). For all movement types, the similarities of the cell ensembles that were active on different bouts of the same movement type were significantly greater than those of the ensembles that were active during the baseline periods before each bout. $^{\#}P < 0.05$; Kolmogorov–Smirnov test, corrected for multiple comparisons using a Benjamini–Hochberg procedure with a false-discovery rate of 0.05. Off-diagonal asterisks indicate that the neural ensembles that were active during bouts of two different movement types were significantly less similar to each other than the ensembles activated on different bouts of the same movement type, for both of the two movement types under consideration. $^{*}P < 0.05$; Kolmogorov–Smirnov test, corrected for multiple comparisons using a Benjamini–Hochberg procedure with a false-discovery rate of 0.05. **e**, The cumulative distribution functions show the range of ensemble similarity values for the dSPN and iSPN ensembles that were activated on two bouts of the same movement type or on two bouts of different movement types (as described in **d**). For both iSPNs and dSPNs, ensemble similarity values were significantly lower for two bouts of different movement types than for two different bouts of the same movement type. $P < 0.01$; Kolmogorov–Smirnov test. **f**, Mean pairwise distances between the individual dSPNs or iSPNs activated on bouts of two different movement types. We normalized the values by comparing the mean weighted distance between the cells that were active during the two movement types to the same quantity determined under the null hypothesis that the spatial probability distributions of active cells on the two movement types were the same. For the latter determination, we created shuffled datasets in which we randomly permuted the firing rate of each cell between the two movement types, and we averaged the results over twenty-five different shuffled datasets. We normalized each distance value by taking the actual mean value, subtracting the mean value determined under the null hypothesis, and then dividing this difference by the standard deviation of the distance across the twenty-five shuffled datasets (Methods). Asterisks indicate that the mean pairwise distance was significantly greater than that expected by chance, indicating that the two movement types activated spatially distinguishable cell ensembles. $^{*}P < 0.05$; Wilcoxon signed-rank test, corrected for multiple comparisons using a Benjamini–Hochberg procedure with a false-discovery rate of 0.05. Plots in **d**–**f** are based on $n = 102$ and $n = 126$ comparisons between bouts of the same movement type, and 255 and 315 comparisons of bouts of different movement types, in *Drd1a*^{cre} and *Adora2a*^{cre} mice, respectively. Values are from $n = 17$ *Drd1a*^{cre} mice and $n = 21$ *Adora2a*^{cre} mice, aggregated over the 1-h recordings on day −5 and the 30-min recordings performed on days −4 to −1 after saline vehicle injection but before drug administration.

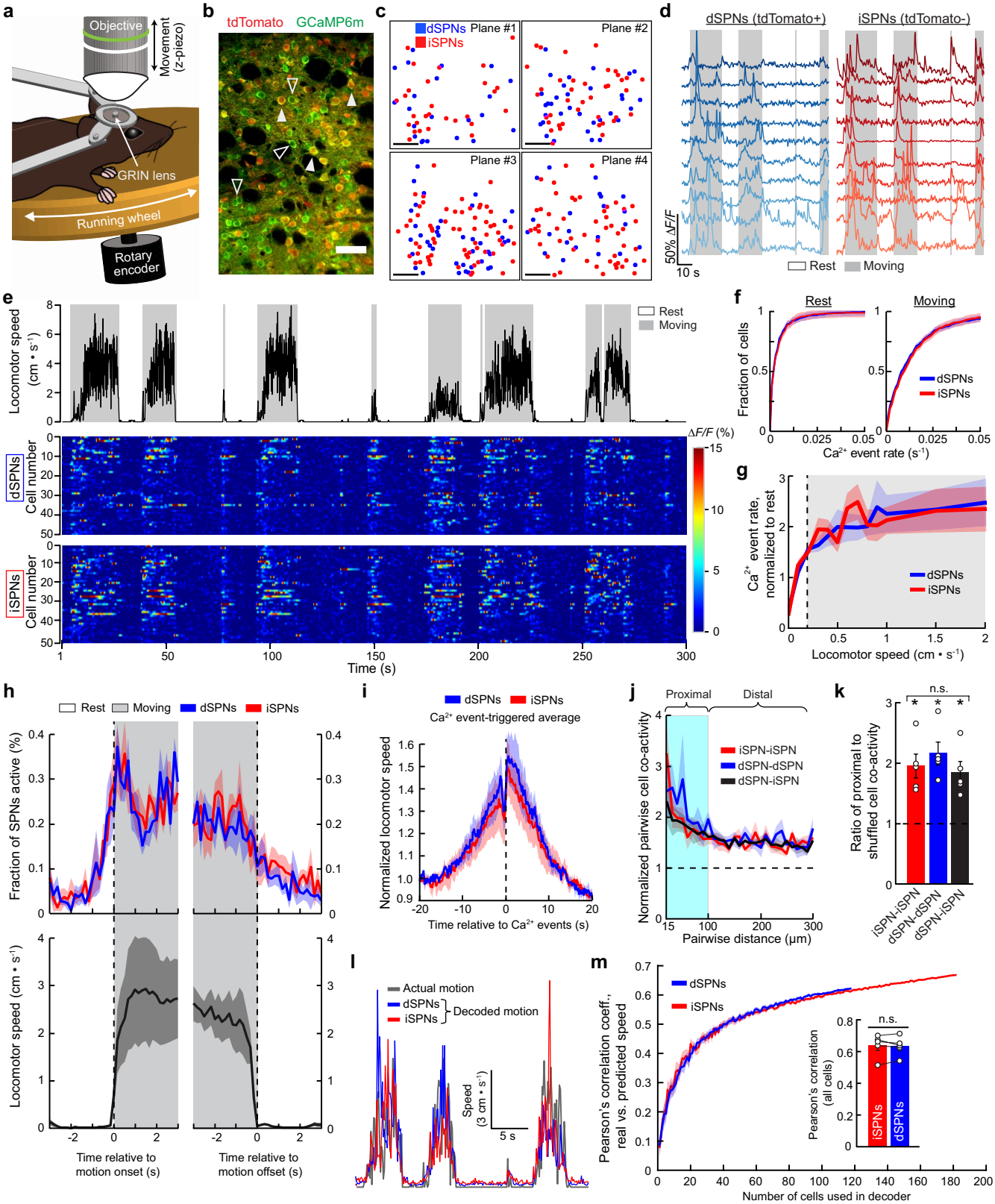

Extended Data Fig. 4 | See next page for caption.

Extended Data Fig. 4 | Simultaneous recordings of dSPNs and iSPNs show that the two cell types encode movement with indistinguishable spatiotemporal patterns of activation. **a**, To image dSPN and iSPN Ca^{2+} activity concurrently, we prepared mice that expressed GCaMP6m in both cell types but tdTomato only in dSPNs (Methods). Mice were head-fixed on a running wheel beneath the objective lens of a two-photon microscope. A piezoelectric actuator moved the axial position of the objective to allow volumetric imaging across four planes at different depths of the tissue (15-μm axial spacing). The mice were free to run or rest on the wheel (Supplementary Video 3). We tracked the motion of the wheel using a rotary encoder (500 encoder pulses per revolution) that provided a read-out of the instantaneous locomotor speed. We computed the mean speed of the mouse at a time-resolution matching that of the two-photon volume acquisition rate (6 Hz, or 166 ms per time bin). We identified periods of movement by marking all time bins in the mean speed trace with values $>0.2\,cm\,s^{-1}$. To identify instances of motion onset, we selected all time bins for which speeds were $<0.2\,cm\,s^{-1}$ for at least 1 s in the immediately prior time bins, and $>0.2\,cm\,s^{-1}$ for at least 1 s in the immediately subsequent time bins. To identify instances of motion offset, we used the opposite criterion. **b**, Histological section of dorsomedial striatum expressing tdTomato (red) in *Drd1a*^{cre} positive cells and immunostained for GFP (green) to visualize GCaMP6m expression. Closed arrowheads point to three example dSPNs that expressed both GCaMP6m and tdTomato. Open arrowheads point to three putative iSPNs that expressed GCaMP6m but not tdTomato. Scale bar, 50 μm. **c**, Representative cell maps from each of the four imaging planes in an example mouse with 118 detected dSPNs (blue) and 183 detected iSPNs (red). Scale bars, 100 μm. **d**, Representative traces of Ca^{2+} activity from 10 dSPNs (blue) and 10 iSPNs (red) from the same mouse as in **c**. Grey shading here and in **e**, **g**, **h** denotes periods classified as movement on the running wheel. **e**, Locomotor speed on the running wheel (top) and Ca^{2+} activity traces of individual dSPNs (middle) and iSPNs (bottom), during part of an imaging session in an example mouse. Note the clear correlation between locomotion and Ca^{2+} activity in both cell types. **f**, Mean cumulative distribution functions of Ca^{2+} event rates in dSPNs ($n = 699$) and iSPNs ($n = 1020$) were nearly identical, during periods of rest (left) and running (right). **g**, Mean Ca^{2+} event rates in dSPNs and iSPNs as a function of mouse locomotor speed. Events rates are shown normalized to their mean levels when the mice were resting (speed $<0.2\,cm\,s^{-1}$). Grey shading denotes speeds at which we classified the mouse as moving ($>0.2\,cm\,s^{-1}$). **h**, Mean locomotor speed (bottom) and the fraction of SPNs that are activated (top), plotted as a function of time relative to motion onset (left) and offset (right). We determined the onset time of neural activity as the time at which the mean percentage of active cells was ≥ 3 s.d. of the percentage of active cells during the baseline periods of −3 to −1 s relative to motion onset. Using this criterion, dSPNs and iSPNs respectively activated -666 ± 97 ms and -733 ± 51 ms before motion onset (mean ± s.e.m; $n = 5$ mice; Methods), which were statistically indistinguishable. $P = 0.9$; Wilcoxon rank-sum test. **i**, Mean locomotor speed as a function of time relative to the occurrences of Ca^{2+} events in dSPNs and iSPNs. For each cell, we normalized these traces to the mean speed 20 s before Ca^{2+} excitation, then averaged the traces across all cells of each type and all mice. **j**, Mean pairwise coactivity (Methods) for dSPN–dSPN, iSPN–iSPN and dSPN–iSPN cell pairs, computed as a function of the distances between the pairs of cells, normalized to coactivity values in temporally shuffled datasets (1,000 distinct shuffles) in which time-correlated activity patterns were scrambled. Cyan shading indicates proximal (20–100 μm) cell pairs. Data are from periods of movement on the running wheel. **k**, Pairwise coactivity values (mean ± s.e.m.) were significantly greater for proximal cell pairs than those in temporally shuffled datasets (*$P < 0.05$; Wilcoxon rank-sum test; $n = 5$ mice), and did not depend on the SPN types. n.s. denotes $P > 0.05$; Wilcoxon rank-sum test. Data points from individual mice are shown as open circles. **l**, We created GLMs to make time-dependent predictions of mouse locomotor speed based on the $\Delta F(t)/F_0$ activity traces of the cells determined by two-photon Ca^{2+} imaging. We used the GLM libraries in MATLAB (Mathworks), using a Gaussian noise model and taking the identity function as the linking function. We used 70% of the time bins in the set of $\Delta F(t)/F_0$ traces for training the GLM, and 30% for testing it. To study the accuracy of the speed predictions as a function of the number of cells (n) included in the GLM, for each value of n, we randomly chose n cells from the total available, constructed the GLM and computed the Pearson's correlation coefficient between the actual and predicted speed traces. For each n value, we repeated this procedure with 10 different randomly chosen subsets of cells and then computed the mean correlation coefficient of the real and predicted speeds across the 10 different sub-samplings. In an example mouse, traces of the actual running speed (grey) were well fit by models based on the activity of either dSPNs (blue) or iSPNs (red). **m**, Mean Pearson correlation coefficients for an example mouse between the actual and predicted running speeds, for GLMs based on either dSPNs or iSPNs (10 sets of randomly chosen cells for each abscissa value, out of 301 total cells). Inset shows the correlation coefficients (mean ± s.e.m.) from $n = 5$ mice, computed using either 115 dPSNs or 115 iSPNs from each mouse. Data points from individual mice are shown as open circles and were statistically indistinguishable across the two cell types. $P = 0.13$; Wilcoxon signed-rank test. **f**–**j**, Colour shading denotes s.e.m. for $n = 5$ *Drd1a*^{cre} × Ai14 mice.

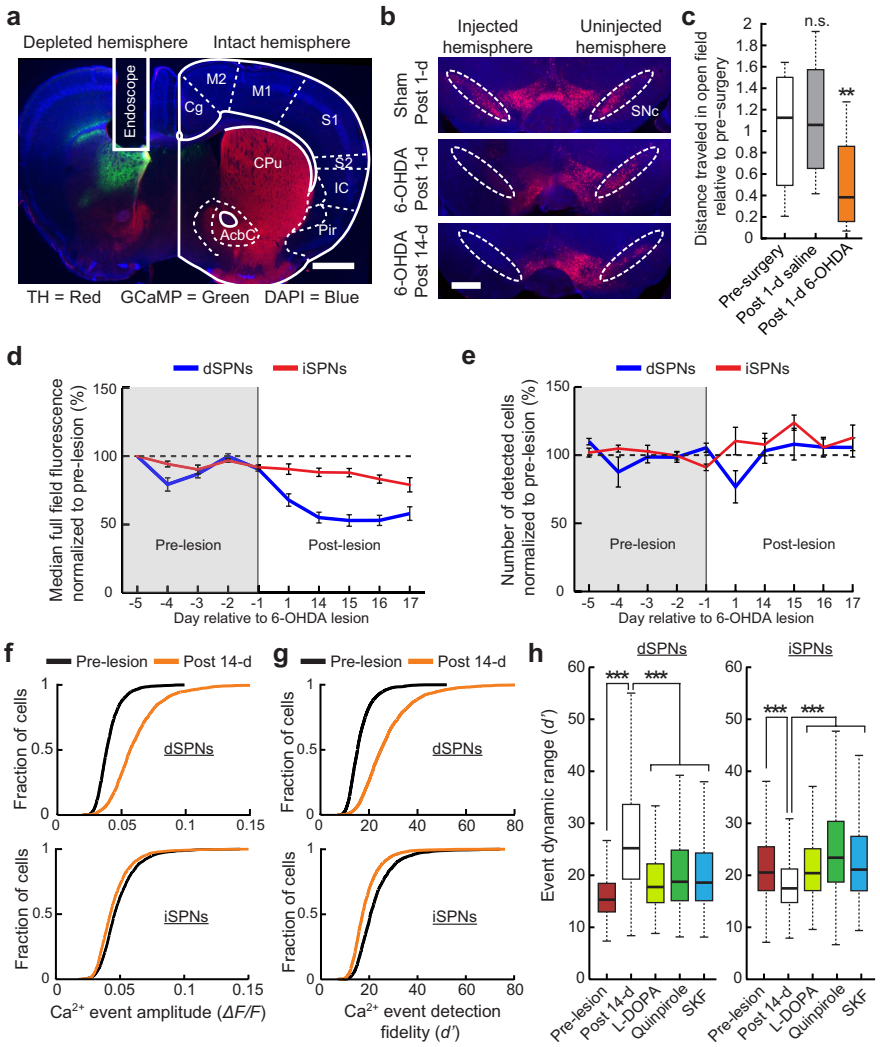

Extended Data Fig. 5 | See next page for caption.

Extended Data Fig. 5 | 6-OHDA injections rapidly ablate SNc dopamine neurons and disrupt motor behaviour without impairing the fidelity of Ca^{2+} event detection. a, Example coronal brain section from an experimental mouse, immunostained for GCaMP6m (anti-GFP, green) and tyrosine hydroxylase (anti-TH, red). DAPI was used to stain the nuclei (blue). White lines demarcate the position of the implanted microendoscope, and the boundaries of nearby brain areas. AcbC, accumbens core; Cg, cingulate cortex; CPu, caudate/putamen; IC, insular cortex; M1 and M2, motor cortices; Pir, piriform cortex; S1 and S2, somatosensory cortices. Labels are adapted from an anatomical atlas of the mouse brain[38]. Scale bar, 1 mm. **b**, Representative midbrain coronal sections acquired 1 day after unilateral infusions of saline (top) or 6-OHDA (middle), or >14 days after 6-OHDA infusion (bottom), and then immunostained for tyrosine hydroxylase (red). DAPI was used to stain the nuclei (blue). Dopamine cell bodies are absent in the SNc of mice that received 6-OHDA, at both 1 and >14 days after 6-OHDA infusion. Scale bar, 500 μm. **c**, 24 h after infusions into SNc of 6-OHDA but not of saline, mice exhibited disrupted patterns of spontaneous locomotion in an open field arena. $P = 4 \times 10^{-3}$ for 6-OHDA and $P = 0.8$ for saline; $n = 7$ saline-treated and 14 6-OHDA-treated mice; Wilcoxon signed-rank test for comparisons to the pre-lesion behaviour of each mice. **d**, The median fluorescence intensity across the entire imaging field (normalized to pre-lesion values on day −5 for each mouse and then averaged across mice) decreased significantly after 6-OHDA lesions in mice of both genotypes. $P < 10^{-7}$ comparing median fluorescence intensities (normalized to pre-lesion means) averaged across 5 days before versus 5 days after lesion; Wilcoxon rank-sum test. However, fluorescence intensities stabilized 15–17 days after the 6-OHDA lesion, and there were no further significant changes over time in either mouse line. $P > 0.05$; $n = 5$ *Drd1a*^{cre} and 7 *Adora2a*^{cre} mice; Spearman correlation. Error bars indicate s.e.m. for 5 *Drd1a*^{cre} and 7 *Adora2a*^{cre} mice. **e**, The number of active SPNs (mean ± s.e.m.) detected in total on each day of the study, normalized to the mean value (dashed horizontal line) detected before 6-OHDA infusion (days shaded grey). On days on which mice received drug treatments (Fig. 1a), the data shown here are from the initial portions of the recording sessions before drug administration. The number of active cells was stable across the study, except for a single pairwise difference in the number of active iSPNs. Friedman ANOVA; $n = 5$ *Drd1a*^{cre} and $n = 7$ *Adora2a*^{cre} mice; $P > 0.05$ for *Drd1a*^{cre} and $P = 0.01$ for *Adora2a*^{cre}; $P = 5 \times 10^{-4}$ for post hoc test comparing the number of iSPNs detected 1 day before the lesion and 15 days after the lesion; Fisher's least significant difference test with a Holm–Bonferroni correction for multiple comparisons. **f**, Cumulative distributions of peak $\Delta F/F$ values for Ca^{2+} events from individual dSPNs (top) and iSPNs (bottom), before and after 6-OHDA lesion. After the lesion, Ca^{2+} event amplitudes were significantly greater in dSPNs (3.7 ± 0.02% (pre-lesion) versus 6.0 ± 0.03% (14 days after)), but smaller in iSPNs (4.4 ± 0.02% (pre-lesion) versus 4.0 ± 0.02% (14 days after)). Data are mean ± s.e.m.; $P < 10^{-10}$ for both SPN types; Wilcoxon rank-sum test. Data in **f** and **g** are from $n = 3{,}332$–$3{,}734$ dSPNs or iSPNs, from before (day −5) or 14 days (day 14) after 6-OHDA lesion, in $n = 12$ *Drd1a*^{cre} mice and 13 *Adora2a*^{cre} mice, respectively. **g**, Cumulative distributions of the signal detection fidelity (d') of Ca^{2+} events in individual dSPNs (top) and iSPNs (bottom), before and after 6-OHDA lesion. Owing to the decrease in background fluorescence intensity, Ca^{2+} events in dSPNs became easier to detect after 6-OHDA lesion, as quantified by the increase in d' values for dSPNs. $d' = 17 \pm 0.1$ (mean ± s.e.m.; pre-lesion) versus 29 ± 0.2 (14 days after). The changes in d' values for iSPNs were smaller in magnitude ($d' = 22 \pm 0.1$ (pre-lesion) versus 19 ± 0.1 (14 days after)), while keeping the optical conditions for Ca^{2+} event detection extremely favourable. Crucially, all changes in Ca^{2+} event detection fidelity values were opposite to those observed for Ca^{2+} event rates in the two cell types (Fig. 3), and thus cannot account for the event rate changes. **h**, d' values for Ca^{2+} events from individual dSPNs (left) and iSPNs (right), before and after 6-OHDA lesions, and after drug treatments in mice following 6-OHDA lesion. d' values increased after 6-OHDA lesions and decreased after the drug treatments in dSPNs. By contrast, d' values decreased after 6-OHDA lesions and increased after drug treatment in iSPNs. $^{***}P < 10^{-10}$ for all conditions in both genotypes; Wilcoxon rank-sum test; values are from $n = 1{,}770$–$2{,}027$ dSPNs from 5 *Drd1a*^{cre} mice and $n = 1{,}719$–$2{,}393$ iSPNs from 6 *Adora2a*^{cre} mice, recorded before (day −5) and after 6-OHDA lesion (day 14), or after the lesion and quinpirole (day 16), SKF81297 (day 18) and L-DOPA (day 20) treatments. As in **g**, these changes in d' have an opposite sign to the changes in Ca^{2+} event rates (Fig. 4), and thus cannot account for the latter effects. Throughout the study, d' values remained extremely high, in that a d' value >16 corresponds mathematically to a mean rate of $<10^{-10}$ errors in Ca^{2+} event detection per hour. This nearly vanishing predicted error rate is unattainable experimentally over many hours of recording but underscores the highly favourable conditions for Ca^{2+} imaging.

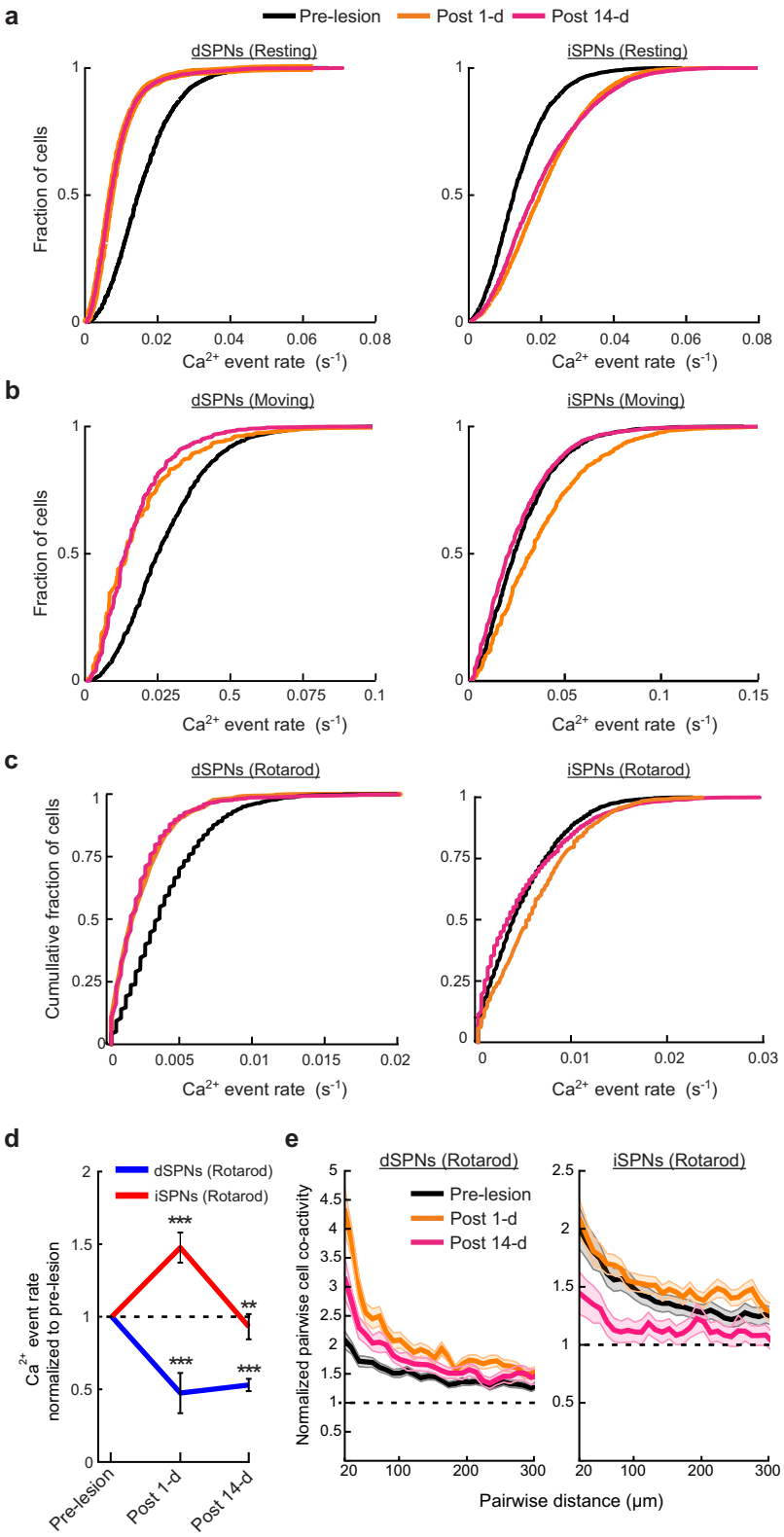

Extended Data Fig. 6 | See next page for caption.

Extended Data Fig. 6 | Lesion of dopamine neurons altered Ca^{2+} event rates in dSPNs and iSPNs during spontaneous open field exploration and forced movement on the rotarod. a, **b**, Cumulative probability distributions of Ca^{2+} event rates in dSPNs (left) and iSPNs (right) while mice were resting (**a**) or in locomotion (**b**) before the lesion of dopamine neurons, 1 day after the lesion (day 1), and >14 day after the lesion (day 14). Ca^{2+} event rates in dSPNs were depressed at both time points after the lesion, during rest and locomotion. Ca^{2+} event rates in iSPNs were elevated at both time points after the lesion when mice were resting. However, when the mice were moving, iSPN activity rates were elevated at 1 day but not >14 days after the lesion, compared to values from before the lesion. The distributions of Ca^{2+} event rates in dSPNs in resting mice were nearly identical at 1 and >14 days, making it hard to visually distinguish the two plots. Data are from 12 *Drd1a*^{cre} mice and 13 *Adora2a*^{cre} mice. The *Drd1a*^{cre} mice yielded a total of 2,554–3,732 activated dSPNs during movement and rest, across the different days of the study, whereas the *Adora2a*^{cre} mice yielded 3,209–3,702 iSPNs. All comparisons within each SPN type between Ca^{2+} event rates from before the lesion to those 1 d and 14 d after the lesion were significant. $P < 10^{-3}$; Wilcoxon rank-sum test. **c**, Cumulative distribution functions of Ca^{2+} event rates in individual dSPNs and iSPNs as mice walked on the rotarod. At 1 day after dopamine depletion (day 1), Ca^{2+} event rates were reduced in dSPNs and increased in iSPNs. At >14 days after dopamine depletion (day 14), Ca^{2+} event rates were still reduced in dSPNs but in iSPNs were at or even slightly below normal values. Data pre-lesion and >14 days after dopamine depletion are based on 5 *Drd1a*^{cre} mice and 7 *Adora2a*^{cre} mice; however, 1 day after dopamine depletion only 2 *Drd1a*^{cre} mice and 3 *Adora2a*^{cre} mice could perform the rotarod assay without falling off, precluding determinations of Ca^{2+} event rates from the other mice on that day. All comparisons within each SPN type between Ca^{2+} event rates from before the lesion to those 1 and >14 days after the lesion were highly significant ($P < 10^{-10}$; Wilcoxon rank-sum test), except for the comparison of iSPN activity rates from before the lesion to those >14 days after ($P = 5 \times 10^{-3}$; Wilcoxon rank-sum test). **d**, Rates of Ca^{2+} events (mean ± s.e.m.) as mice walked on the rotarod, normalized to the corresponding values from before dopamine depletion. dSPN activation rates were substantially reduced at both time points after the lesion. iSPN event rates were substantially increased 1 day after the lesion (day 1), but had returned to near baseline levels by 14 days after the lesion (day 14), mirroring the effects of dopamine depletion on dSPN and iSPN activity during spontaneous movement (see Fig. 3f). $^{**}P < 5 \times 10^{-3}$ and $^{***}P < 5 \times 10^{-7}$; Wilcoxon rank-sum test. Owing to the large numbers of Ca^{2+} events across thousands of SPNs that contributed to these calculations, the slight depression of Ca^{2+} event rates in iSPNs at 14 days after the lesion was statistically significant. **e**, The extent of pairwise coactivation of dSPNs (left) and iSPNs (right) during the rotarod assay, as a function of the pairwise distance between cells, before dopamine depletion, at 1 and >14 days after dopamine depletion. Values are normalized to those attained from shuffled datasets in which the times of the Ca^{2+} events of each cell were randomized (Methods). The spatial clustering of activity in proximal iSPN pairs (20–100 μm apart) was significantly reduced 14 days after the lesion, relative to values from beforehand. $P < 10^{-16}$; Wilcoxon rank-sum test; $n = 7$ *Adora2a*^{cre} mice. Shaded areas denote s.e.m. Data and statistical tests in **c**–**e** are from 1,930, 712 and 1,672 dSPNs and 1,731, 853 and 1,607 iSPNs that were active during the rotarod assay pre-lesion, 1 (day 1), and 14 (day 14) days after the lesion, respectively.

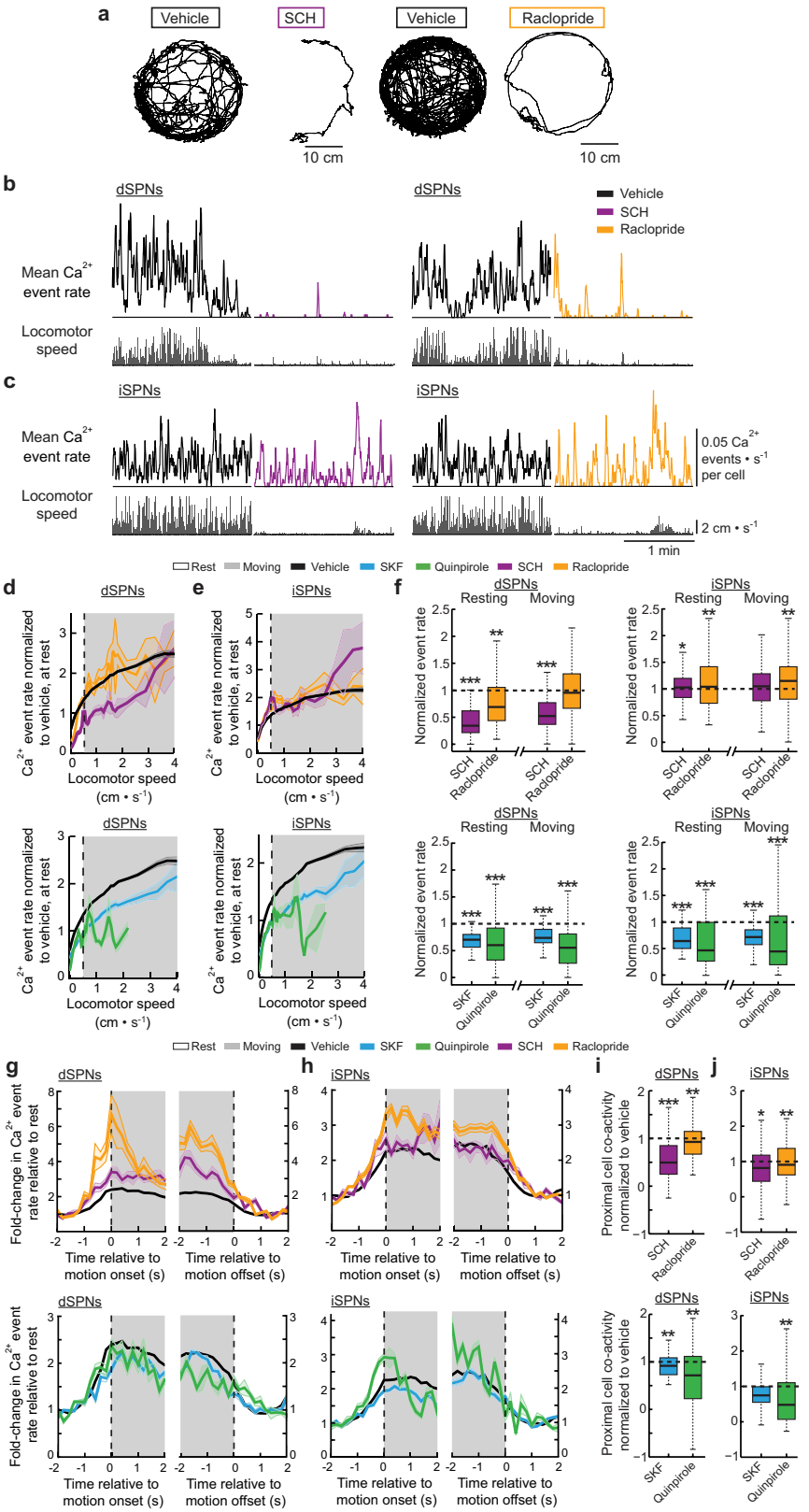

Extended Data Fig. 7 | See next page for caption.

Extended Data Fig. 7 | In healthy mice, D1R or D2R antagonists affect SPN activity similarly to an acute (but not chronic) loss of dopamine neurons, whereas dopamine receptor agonists have divergent effects from those observed in dopamine-depleted mice. a–c, Example locomotor trajectories (15-min duration) of mice moving freely within a circular arena (**a**) and paired example traces of mouse locomotor speed and the mean rate of Ca^{2+} events in dSPNs (**b**) and iSPNs (**c**) after administration of saline vehicle or a selective antagonist of D1Rs (SCH23390, 0.2 mg kg^{-1}) or D2Rs (raclopride, 1 mg kg^{-1}). Both drugs reduced locomotion relative to vehicle. $P = 10^{-4}$; Wilcoxon signed-rank test; $n = 18$ mice. **d**, **e**, Mean Ca^{2+} event rates in dSPNs (**d**) and iSPNs (**e**) as a function of locomotor speed, following administration of saline vehicle, a D1R- or D2R-selective antagonist (0.2 mg kg^{-1} SCH23390 or 1 mg kg^{-1} raclopride, respectively) (top) or a D1R- or D2R-selective agonist (1 mg kg^{-1} SKF81297 or 1 mg kg^{-1} quinpirole, respectively) (bottom). Rates are normalized to cell population means when mice were at rest (<0.5 cm s^{-1}) after vehicle injection (Methods). Colour shading surrounding each curve denotes s.e.m. **f**, SPN Ca^{2+} event rates during rest and movement after treatment with a dopamine-receptor antagonist or agonist. The D1R antagonist (SCH23390) reduced dSPN but not iSPN activity. The D2R antagonist (raclopride) increased iSPN but not dSPN activity. Both agonists (quinpirole, SKF81297) reduced activity in both SPN types during rest and movement. $*P < 0.05$, $**P < 5 \times 10^{-3}$, $***P < 5 \times 10^{-7}$; Wilcoxon signed-rank test comparing all drug conditions to saline vehicle injection; $n = 14$ speed bins per mouse in the resting state (<0.5 cm s^{-1}) and 24 speed bins per mouse in the moving state (>0.5 cm s^{-1}); $n = 7$ *Drd1a*^{cre} and 11 *Adora2a*^{cre} mice. **g**, **h**, Mean Ca^{2+} event rates in dSPNs (**g**) and iSPNs (**h**) relative to motion onset (left) and offset (right) following administration of saline vehicle, SCH23390 or raclopride (top), or SKF81297 or quinpirole (bottom). Traces are normalized to cell population means averaged over the time period from −2 to −1 s preceding motion onset. Raclopride increased dSPN ($P = 6 \times 10^{-11}$) and iSPN ($P = 2 \times 10^{-9}$) activation at motion onset. Wilcoxon rank-sum test; comparing 11 time bins for the interval of 0–2 s after motion onset to the baseline periods in each of the 7 *Drd1a*^{cre} and 11 *Adora2a*^{cre} mice. SCH23390 slightly altered dSPN ($P = 0.02$) but not iSPN activation ($P = 0.4$) at motion onset. In *Drd1a*^{cre} mice, there were $n = 1{,}917$ (vehicle), 134 (SCH23390) and 129 (raclopride) instances of motion onset, whereas in *Adora2a*^{cre} mice there were 2,798 (vehicle), 155 (SCH23390) and 233 (raclopride) such instances. Colour shading surrounding each curve denotes s.e.m. **i**, **j**, Coactivity of proximal (20–100 μm apart) dSPN (**i**) or iSPN (**j**) cell pairs during periods of movement, following administration of saline vehicle, SCH23390 or raclopride (top) or saline, SKF81297 or quinpirole (bottom). Coactivity values are plotted after subtraction of the coactivity values determined for temporally shuffled datasets under the same drug treatment conditions, and then normalized to the values attained for saline administration. Comparing measured values for each drug to those attained with saline; $*P < 0.05$, $**P < 5 \times 10^{-3}$ and $***P < 5 \times 10^{-7}$; Wilcoxon signed-rank test; 8 spatial bins of cell–cell separation for each of the $n = 7$ *Drd1a*^{cre} and $n = 11$ *Adora2a*^{cre} mice. **d**–**j**, Data are based on the same 7 *Drd1a*^{cre} and 11 *Adora2a*^{cre} mice. Figure 1a shows the schedule of drug treatments. Data acquired in the 30-min Ca^{2+} imaging sessions after drug administration have been normalized for each mouse to the values determined on the same day during the 30-min Ca^{2+} imaging sessions occurring after saline vehicle administration but before drug treatment.

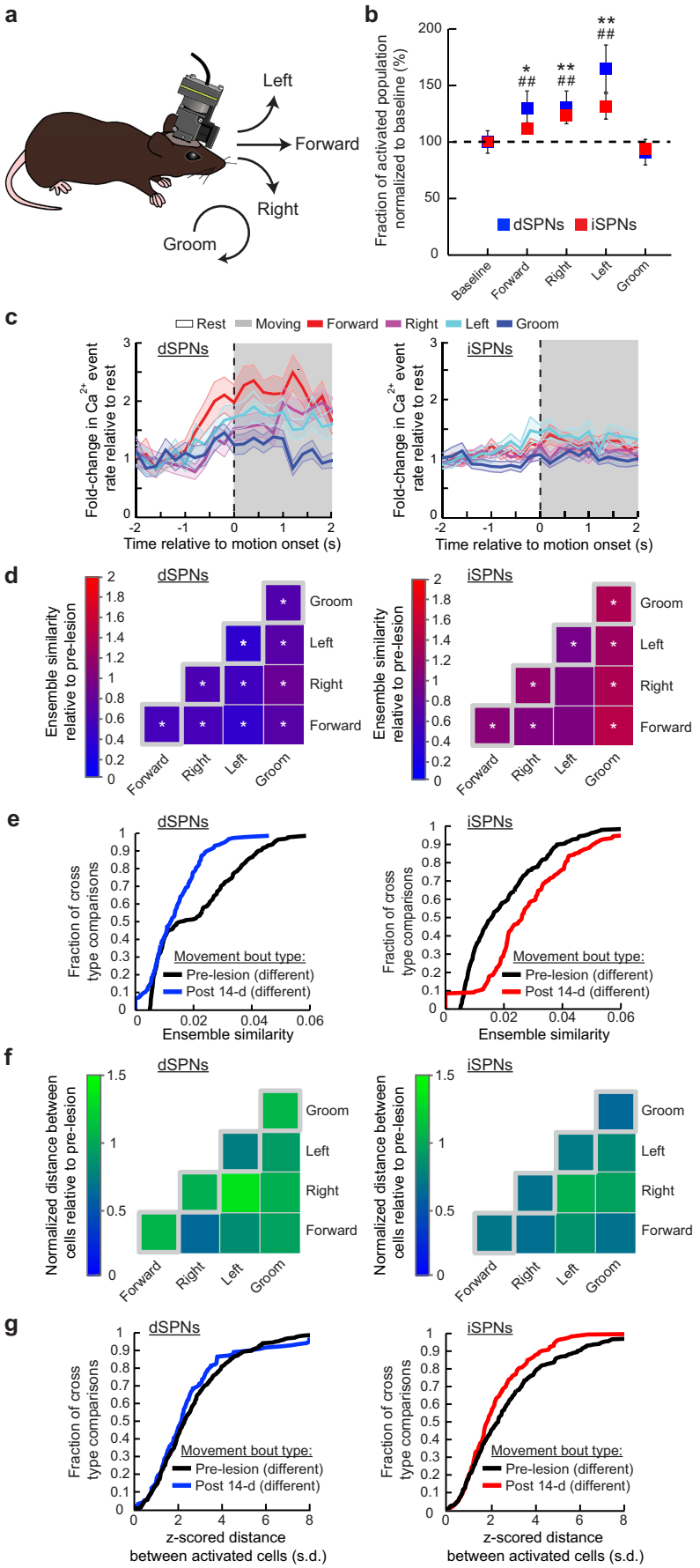

Extended Data Fig. 8 | See next page for caption.

Extended Data Fig. 8 | Dopamine depletion reduces the movement-type specificity of iSPN activity patterns. a, Following dopamine depletion, we classified mouse movement bouts into different types, as in Extended Data Fig. 3. After 6-OHDA lesion, there were insufficient bouts of upward rearing to allow statistical analyses. **b**, Percentages of SPNs (mean ± s.e.m.) that exhibited Ca^{2+} activity, relative to the baseline periods (dashed line) immediately before each movement type, >14 days after 6-OHDA lesion. Compared to baseline periods, there was a significant increase in dSPN and iSPN activity for all movement types, except during grooming. $*P < 0.05$ and $**P < 5 \times 10^{-3}$ for dSPNs; $\#P < 0.05$ and $\#\#P < 5 \times 10^{-3}$ for iSPNs; Wilcoxon signed-rank test. Data in **b** and **c** are based on 206 forward movements, 200 right turns, 290 left turns and 314 grooming bouts in 13 *Drd1a*^{cre} mice and 331 forward movements, 295 right turns, 194 left turns and 339 grooming bouts in 21 *Adora2a*^{cre} mice. **c**, Rates of Ca^{2+} events (mean ± s.e.m.) in dSPNs and iSPNs as a function of time relative to the onsets of different types of movements, >14 days after 6-OHDA lesion. Event rates are shown normalized to the values from −2 to −1 s before motion onset. As found when all movements were grouped together (Fig. 3g), the rates of iSPNs hardly increase at motion onset in parkinsonian mice. **d**, Mean values of the neural ensemble similarity computed for the sets of dSPNs and iSPNs that were active during pairs of bouts of either the same (on-diagonal) or different (off-diagonal) types of movements, in freely behaving mice >14 days after 6-OHDA lesion (Methods). For each pair of movement types, values are shown normalized to the corresponding value found in healthy mice before 6-OHDA lesion. Asterisks indicate a significant difference between the pre- and post-lesion values. $*P < 0.05$; Wilcoxon rank-sum test, corrected for multiple comparisons using a Benjamini–Hochberg procedure with a false-discovery rate of 0.05. **e**, Cumulative distribution functions showing the range of ensemble similarity values for the sets of dSPNs and iSPNs that activated on two bouts of different movement types. The similarity of the dSPN ensembles activated on different movement types decreased significantly after 6-OHDA, indicating that the representations of different movements became more distinct. $P < 0.05$; Kolmogorov–Smirnov test. By comparison, the iSPN ensembles activated on different types of movements became more similar after 6-OHDA lesion, consistent with a reduction in the selectivity of iSPN movement encoding. $P < 0.05$; Kolmogorov–Smirnov test. **f**, Mean pairwise distances between the individual dSPNs or iSPNs activated on bouts of two different movement types, in freely behaving mice >14 days after 6-OHDA lesion. We expressed the values as *z* scores, as described in Extended Data Fig. 3f. For each pair of movement types, we then normalized each *z* score by the corresponding value found in healthy mice before 6-OHDA lesion. **g**, Cumulative distribution functions showing the normalized distances between dSPNs (left) and iSPNs (right) (computed as in **f**) before and after 6-OHDA lesion, for bouts of different movement types. The mean pairwise distances between iSPNs, but not dSPNs, that activated on bouts of different movement types decreased significantly after 6-OHDA lesion, indicating that the iSPN cell ensembles active on the different movement types were less spatially distinguishable after 6-OHDA lesion. $P = 0.02$; Kolmogorov–Smirnov test. Plots in **d**–**g** are based on $n = 102$ and $n = 126$ comparisons between bouts of the same movement type, and 255 and 315 comparisons of bouts of different movement types, in 17 *Drd1a*^{cre} and 21 *Adora2a*^{cre} mice, respectively, before 6-OHDA lesion, and on $n = 72$ and $n = 78$ comparisons between bouts of the same movement type, and 180 and 195 comparisons of bouts of different movement types in 12 *Drd1a*^{cre} and 13 *Adora2a*^{cre} mice, respectively, >14 days after 6-OHDA lesion. The pre-lesion data are the same as in Extended Data Fig. 3. The data >14 days after the lesion are aggregated from the 1-h recordings on day 14 plus the 30-min recordings on day 20 that occurred after saline vehicle injection but before administration of 6 mg kg^{-1} L-DOPA (see Fig. 1a).

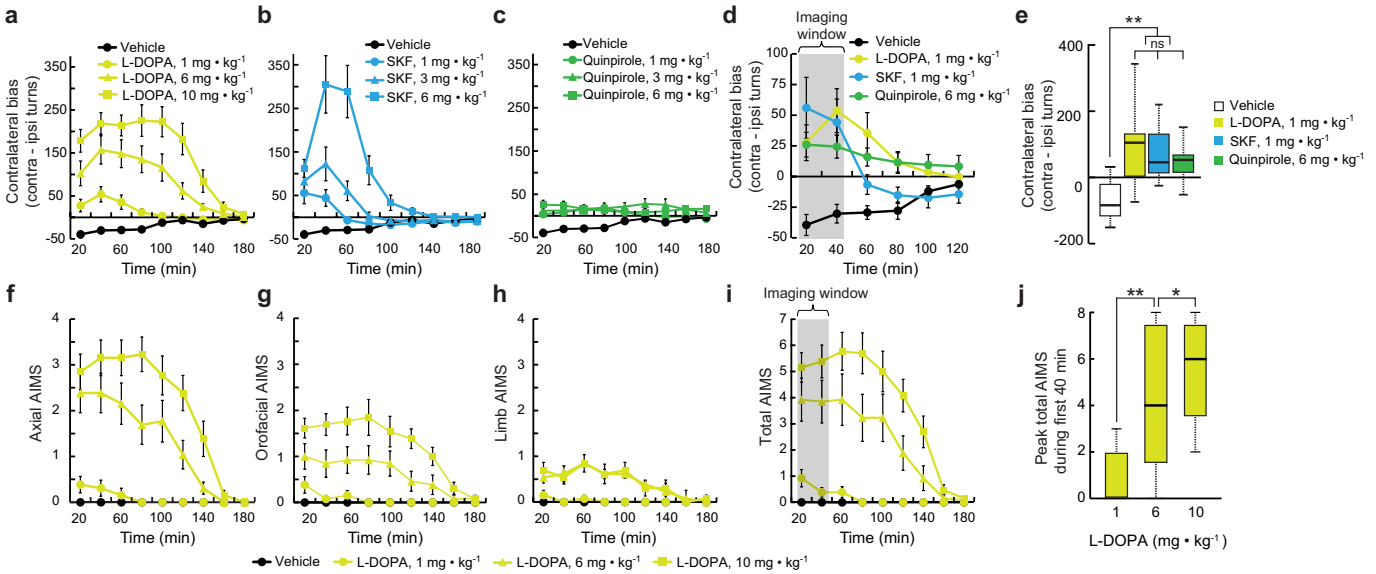

Extended Data Fig. 9 | After unilateral lesion of SNc dopamine cells, L-DOPA and dopamine agonists induce a contralateral turning bias, and L-DOPA can also induce dyskinesia. a–c, Time traces showing mean ± s.e.m. effects of different doses of L-DOPA, SKF81297 and quinpirole on the contralateral rotational bias of mice, scored in 20-min time bins, >14 days after unilateral 6-OHDA lesion. All drug doses had their maximal behavioural effects approximately 30 min after drug administration. All dose–time interactions differed significantly from vehicle treatment ($P < 5 \times 10^{-3}$), and the effects of L-DOPA and SKF81297 were dose-dependent ($P < 5 \times 10^{-3}$). Two-way, repeated-measures ANOVA. **d**, Time traces of the mean ± s.e.m. mouse rotational bias for the three different drugs in **a–c**, at doses of each drug that induce comparable levels of rotational bias during the time window used in our studies for Ca^{2+} imaging (shaded in grey), during which we assessed the effects of these drugs on dSPN and iSPN activity in parkinsonian mice (Fig. 4). **e**, Comparison of the net rotational bias in the first 40 min after administration of the three drugs at the same doses as in **d**. Note that, as assessed by their effects on turning behaviour, these three compounds were statistically indistinguishable at these doses. 'ns' denotes $P > 0.2$ for comparisons between drugs; $n = 13$ mice; Wilcoxon signed-rank test. However, all drugs had significant effects relative to vehicle treatment. $^{**}P < 5 \times 10^{-3}$; Wilcoxon signed-rank test; $n = 13$ mice. **f–i**, Time traces showing how different dosages of L-DOPA affect the mean ± s.e.m. axial (**f**), orofacial (**g**), limb (**h**) and total (**i**) AIMS values, a behavioural measure of dyskinesia in preclinical models of Parkinson's disease[31]. All three L-DOPA doses had significant effects compared to vehicle treatments ($P < 0.02$; two-way ANOVA) and differed significantly in their effects at the different dosages ($P < 0.05$). As in **d**, the grey shading in **i** denotes the time window used for Ca^{2+} imaging (Figs. 4, 5). **j**, L-DOPA increased the peak total AIMS values, in a dose-dependent manner, in the first 40-min after mice received the L-DOPA doses in **f–i**. $^{*}P < 0.05$, $^{**}P < 5 \times 10^{-3}$; Wilcoxon signed-rank test. Error bars in **a–d** and **f–i** indicate s.e.m. All data in **a–j** are from a distinct cohort of $n = 13$ freely moving mice not subject to the protocol of Fig. 1a.

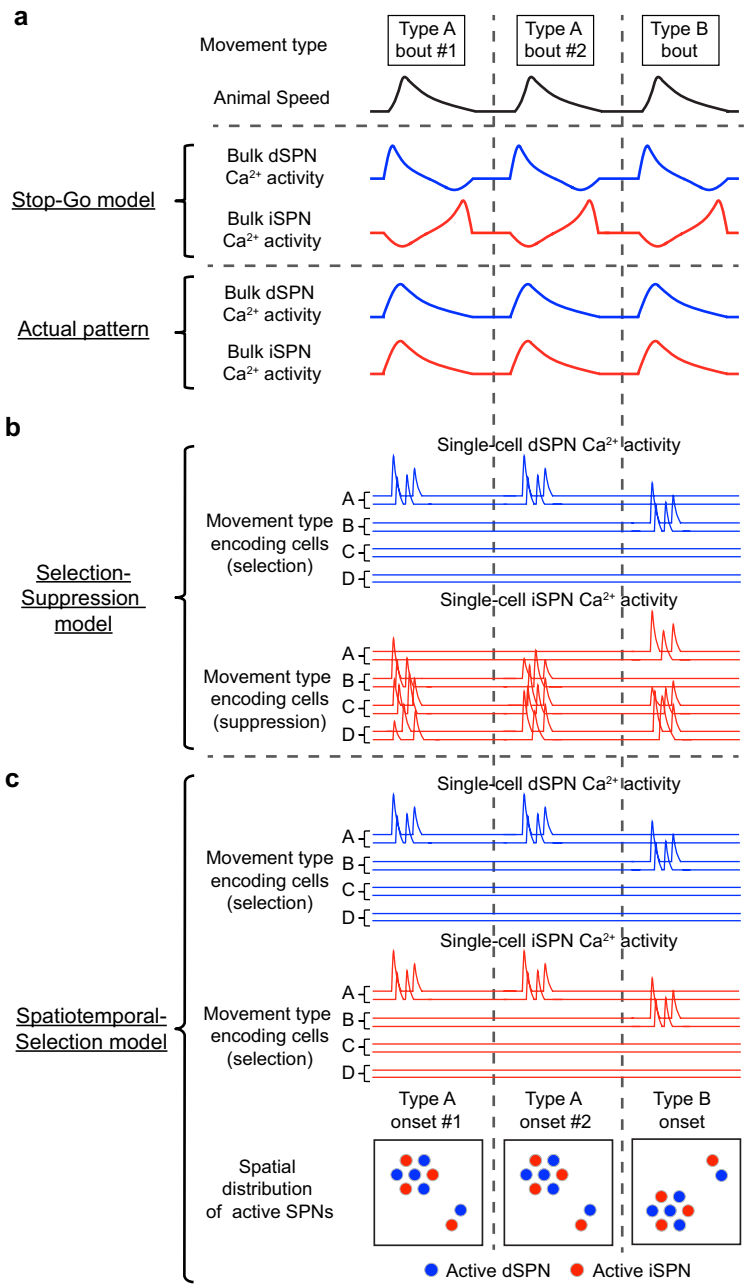

Extended Data Fig. 10 | SPNs encode specific movements via the activation of spatial clusters of cells consisting of both dSPNs and iSPNs. a, Classical models of the basal ganglia, such as the rate model[1,2], posit opposing roles for dSPNs and iSPNs in movement generation. A simple instantiation of these ideas (a 'stop–go' model[11]) predicts increased dSPN and decreased iSPN activity at movement initiation, and decreased dSPN and increased iSPN activity at movement termination. This is depicted here schematically in the traces of aggregate SPN Ca^{2+} activity in the model (middle), relative to motion onset and offset (top). However, in the actual data the activity of both SPN types increases at motion onset and decreases at motion offset (bottom). **b**, Other types of models are more compatible with the concurrent activation of both SPN types at motion onset. In 'suppression–selection' models[15], dSPNs select a motor program, while iSPNs simultaneously suppress competing motor programs. In these models, specific subsets of dSPNs and iSPNs coactivate to select and suppress specific motor programs, respectively. Here we depict this idea using schematic traces of single-cell activity. dSPNs that encode either 'type A' or 'type B' movements activate selectively during one or the other type of movement (see top trace of movements in **a**). By contrast, iSPNs, which suppress competing movements such as those of 'type C' and 'type D', activate on both 'type A' and 'type B' movement bouts. A prediction of this model is that the cell populations encoding different types of movement are more similar (that is, less selective), and possibly more broadly distributed anatomically, for iSPNs than dSPNs. However, the actual data reported here show that the selectivity and spatial distributions of neural responses during movement are comparable in both SPN types (Fig. 2c–e and Extended Data Figs. 3d–f, 4j, k). **c**, More specifically, we found action-selective ensembles in both dSPNs and iSPNs (Extended Data Fig. 3). Unlike the suppression–selection model in **b**, our findings suggest that dSPNs and iSPNs coordinate to select motor programs, depicted here as traces of single-cell activity in which movement 'type A' and 'type B' encoding dSPNs and iSPNs activate selectively on bouts of movement types A and B, respectively (see top trace of movements in **a**). Furthermore, the dSPNs or iSPNs activated for one movement type were physically closer to each other than to SPNs activated for different movement types (Extended Data Fig. 3f). These analyses quantify what is visually apparent in the Ca^{2+} videos of striatal activity, which show that multiple, segregated clusters of coactive dSPNs or iSPNs activate at the onset of motion (Supplementary Videos 1, 2). Finally, using two-photon microscopy to image the simultaneous patterns of Ca^{2+} activity in dSPN and iSPN ensembles, we found that the coactivity of nearby dSPN–iSPN pairs was indistinguishable from that of pairs of the same SPN type (Extended Data Fig. 4). Combining these findings, our data show that different subsets of spatially intermingled dSPNs and iSPNs activate for distinct types of movement (for example, 'type A' and 'type B' movements, bottom depictions of 'spatial distribution').

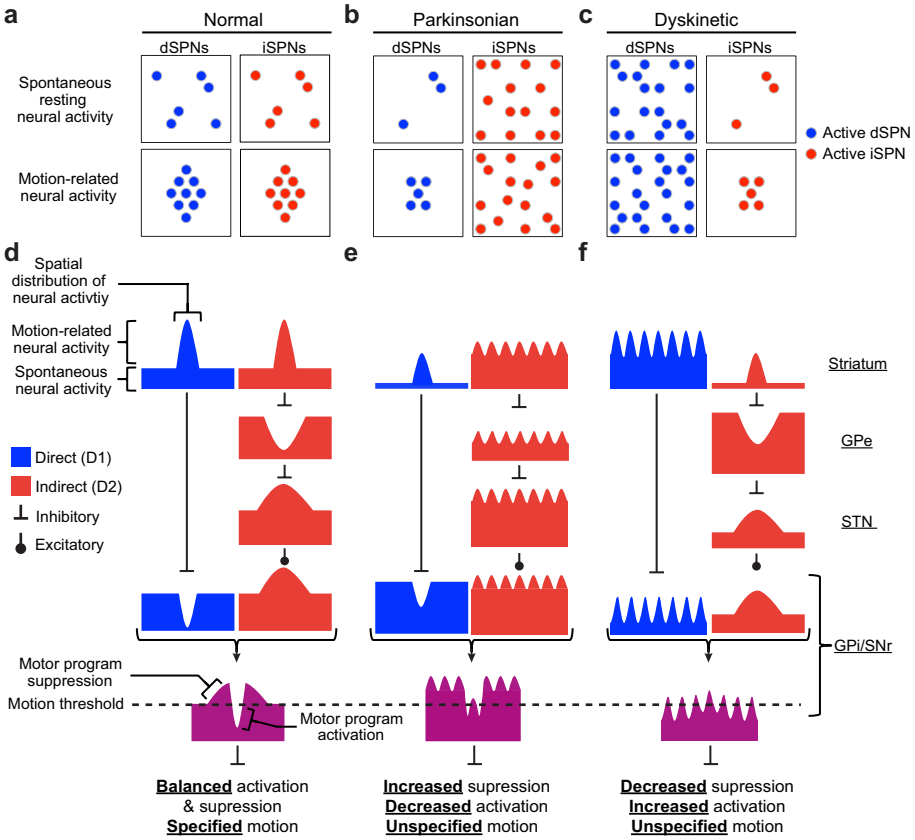

Extended Data Fig. 11 | Implications for basal ganglia dysfunction in parkinsonian and dyskinetic states. a–c, Schematic depictions of the spatial organization of SPN activity. Active cells are shown as filled circles. **a**, Prior to dopamine loss both dSPNs and iSPNs exhibit spatially clustered patterns of coactivation when mice are resting. Clusters of the two cell types are spatially overlapping (Extended Data Figs. 4, 10). During movement, both cell types undergo an increase in the number of active cells and extent to which activity is spatially clustered. **b**, After dopamine loss dSPN activity decreases in rate but remains spatially clustered in resting mice (Fig. 3e, j). Moreover, dSPNs still coactivate in a spatially clustered manner during movement initiation (Fig. 3g). The rate of iSPN activity is increased after dopamine depletion in resting mice (Fig. 3e). However, iSPNs are less responsive at the onset of and throughout movement, and their motion-related activity shows almost no spatial clustering (Fig. 3g–j). **c**, During L-DOPA-induced dyskinesia (LID), dSPNs are hyperactive, unresponsive to movement, and spatiotemporally decorrelated (Fig. 5c–h), much like iSPNs after dopamine loss. During LID, iSPNs are hypoactive but retain their movement-related activation and spatial clustering (Fig. 5c–h), much like dSPNs after dopamine depletion. **d–f**, Iconic depictions of the SPN activity patterns during normal, parkinsonian and dyskinetic states, and the implications for downstream basal ganglia function. Icons are inspired by those in previous work[32]. For each icon in the top row, the height of the rectangular pedestal represents the amplitude of spontaneous SPN activity in resting mice. The height and width of protrusions above the pedestals respectively denote the amplitude and spatial distribution of motion-related SPN activity. On the basis of the known excitatory and inhibitory projections between basal ganglia nuclei, the icons in subsequent rows show the predicted consequences for the downstream neural targets. In these icons, indentations into the rectangular pedestal denote inhibitions of neural activity during active movement. The globus pallidus pars externa (GPe) and the sub-thalamic nucleus (STN) are in the basal ganglia's indirect pathway and receive signals from striatal iSPNs. In the direct pathway, dSPNs project directly to the globus pallidus pars interna and substantia nigra pars reticulata (GPi/SNr), where signals from the two basal ganglia pathways converge (purple icons). GPi/SNr activity influences motor program selection by modulating downstream thalamacortical neurons and brainstem motor nuclei (not depicted). **d**, Before dopamine depletion, GPi/SNr cells receive signals during movement from the direct and indirect pathways that should induce, respectively, spatially structured patterns of neural activation and inhibition in GPi/SNr. We hypothesize that the convergence and spatial patterning of these bidirectional modulations enhance the specificity of the disinhibitory signals transmitted from GPi/SNR (left purple icon). In this view, the spatially coordinated, joint modulation of activity in GPi/SNr by both dSPNs and iSPNs may be crucial for well-choreographed motor programs[15]. **e**, After dopamine depletion, spontaneous activity is reduced in dSPNs and increased in iSPNs. The rate model predicts that these changes in spontaneous activity lead to increases in spontaneous GPi/SNr activity (middle purple icon), tonically suppressing movement. Dopamine depletion also abolishes the spatially clustered, motion-related activation of iSPNs. This added deficit in motion-related iSPN activity is unaccounted for by the rate model and may upset the normal bidirectional spatial patterning of GPi/SNR output activity. This in turn may reduce the specificity of GPi/SNr inhibition, causing abnormal movement specification and motor coordination. **f**, During LID, spontaneous activity rises in dSPNs and declines in iSPNs. The rate model predicts that these changes should tonically drive movement by suppressing GPi/SNr activity (right purple icon). LID also disrupts the amplitude and spatial structure of motion-related dSPN activity. This decorrelated dSPN hyperactivity may disrupt the normally focused suppression of GPi/SNr activity during movement, resulting in increased but less specified movements.

nature research

Corresponding author(s): Prof. Mark Schnitzer

Reporting Summary

Nature Research wishes to improve the reproducibility of the work that we publish. This form provides structure for consistency and transparency in reporting. For further information on Nature Research policies, see Authors & Referees and the Editorial Policy Checklist.

Statistical parameters

When statistical analyses are reported, confirm that the following items are present in the relevant location (e.g. figure legend, table legend, main text, or Methods section).

n/a	Confirmed	
☐	☒	The exact sample size (*n*) for each experimental group/condition, given as a discrete number and unit of measurement
☐	☒	An indication of whether measurements were taken from distinct samples or whether the same sample was measured repeatedly
☐	☒	The statistical test(s) used AND whether they are one- or two-sided *Only common tests should be described solely by name; describe more complex techniques in the Methods section.*
☒	☐	A description of all covariates tested
☐	☒	A description of any assumptions or corrections, such as tests of normality and adjustment for multiple comparisons
☐	☒	A full description of the statistics including central tendency (e.g. means) or other basic estimates (e.g. regression coefficient) AND variation (e.g. standard deviation) or associated estimates of uncertainty (e.g. confidence intervals)
☐	☒	For null hypothesis testing, the test statistic (e.g. *F*, *t*, *r*) with confidence intervals, effect sizes, degrees of freedom and *P* value noted *Give P values as exact values whenever suitable.*
☒	☐	For Bayesian analysis, information on the choice of priors and Markov chain Monte Carlo settings
☒	☐	For hierarchical and complex designs, identification of the appropriate level for tests and full reporting of outcomes
☒	☐	Estimates of effect sizes (e.g. Cohen's *d*, Pearson's *r*), indicating how they were calculated
☐	☒	Clearly defined error bars *State explicitly what error bars represent (e.g. SD, SE, CI)*

Our web collection on statistics for biologists may be useful.

Software and code

Policy information about availability of computer code

Data collection	We acquired video behavior recordings using an open source digital camera driver in (CMU 1394 camera driver) in MATLAB. We acquired two-photon calcium imaging data using open source (Scan Image) software in Matlab. We acquired fluorescence recordings using commercial software for the Inscopix nVista system.
Data analysis	We performed data analysis using custom software written in MATLAB and ImageJ. We also used the Prism (Graphpad) and R programming environments for statistical analyses. The algorithm used for image registration is available on its author's website. The algorithm used for cell sorting is available as supplementary material published elsewhere. Other code will be made available upon request.

For manuscripts utilizing custom algorithms or software that are central to the research but not yet described in published literature, software must be made available to editors/reviewers upon request. We strongly encourage code deposition in a community repository (e.g. GitHub). See the Nature Research guidelines for submitting code & software for further information.

Data

Policy information about availability of data

All manuscripts must include a data availability statement. This statement should provide the following information, where applicable:

- Accession codes, unique identifiers, or web links for publicly available datasets
- A list of figures that have associated raw data
- A description of any restrictions on data availability

Raw data will be made available upon reasonable request.

Field-specific reporting

Please select the best fit for your research. If you are not sure, read the appropriate sections before making your selection.

☒ Life sciences ☐ Behavioural & social sciences

For a reference copy of the document with all sections, see nature.com/authors/policies/ReportingSummary-flat.pdf

Life sciences

Study design

All studies must disclose on these points even when the disclosure is negative.

Sample size	No statistical methods were used for predetermining sample sizes.
Data exclusions	No animals were excluded based on statistical criteria (Please see Methods -> Data analyses and statistical tests). Some mice were excluded from some analyses based on their inability to perform a behavioral task (See Methods -> Rotarod) or based on post hoc histological evaluations of the extent of dopamine cell death (See Methods -> Histology).
Replication	We performed two separate rounds of experimentation that represented replicates covering most of the experiments reported. All of the main findings were highly reproducible.
Randomization	Randomization was not needed for our comparisons between mice of different genotypes.
Blinding	Blinding was not used.

Materials & experimental systems

Policy information about availability of materials

n/a	Involved in the study
☒	☐ Unique materials
☐	☒ Antibodies
☒	☐ Eukaryotic cell lines
☐	☒ Research animals
☒	☐ Human research participants

Antibodies

Antibodies used	We immunostained the tissue sections with antibodies against tyrosine hydroxylase (1:500, Aves TYH) and GFP (1:1000, Molecular Probes A-11122), and then applied fluorophore-conjugated secondary antibodies (Jackson Immunoresearch 703-586-155 and 711-546-152, respectively).
Validation	Primary antibodies were validated in histological brain sections. We validated our tyrosine hydroxylase antibody by its labeling specificity for midbrain dopamine neurons and striatum in the intact (non-lesioned) hemishphere, as compared to the contralateral, dopamine depleted hemisphere. We validated our GFP antibody based on its specificity for labeling at the GCaMP virus injection site.

Research animals

Policy information about studies involving animals; ARRIVE guidelines recommended for reporting animal research

Animals/animal-derived materials	We obtained the GENSAT BAC transgenic Cre driver mouse lines, Drd1a-Cre (FK150) and Adora2a-Cre (KG139), from the Mutant Mouse Research & Resource Centers (www.mmrrc.org). We also used homozygous reporter mice (Ai14; Allen Brain Institute) expressing the red fluorophore tdTomato in a Cre-dependent manner.

We used male and female mice, aged 12–24 weeks at the start of behavioral experiments. The Stanford Administrative Panel on Laboratory Animal Care (APLAC) approved all experiments.

Method-specific reporting

n/a	Involved in the study
☒	☐ ChIP-seq
☒	☐ Flow cytometry
☒	☐ Magnetic resonance imaging